

# A TRIDENT SCHOLAR PROJECT REPORT

NO. 434

---

**An Exploration of Structures in the Transitional Odd-Odd Nucleus Lu-160**

by

Midshipman 1/C Steven T. Hallgren, USN

---



UNITED STATES NAVAL ACADEMY  
ANNAPOLIS, MARYLAND

This document has been approved for public  
release and sale; its distribution is limited.

U.S.N.A. --- Trident Scholar project report; no. 434 (2015)

**AN EXPLORATION OF STRUCTURES IN THE TRANSITIONAL ODD-ODD  
NUCLEUS  $^{160}\text{Lu}$**

by

Midshipman 1/C Steven T. Hallgren  
United States Naval Academy  
Annapolis, Maryland

---

(signature)

Certification of Adviser Approval

Professor Daryl J. Hartley  
Physics Department

---

(signature)

---

(date)

Acceptance for the Trident Scholar Committee

Professor Maria J. Schroeder  
Associate Director of Midshipman Research

---

(signature)

---

(date)

REPORT DOCUMENTATION PAGE				Form Approved OMB No. 0704-0188	
Public reporting burden for this collection of information is estimated to average 1 hour per response, including the time for reviewing instructions, searching existing data sources, gathering and maintaining the data needed, and completing and reviewing this collection of information. Send comments regarding this burden estimate or any other aspect of this collection of information, including suggestions for reducing this burden to Department of Defense, Washington Headquarters Services, Directorate for Information Operations and Reports (0704-0188), 1215 Jefferson Davis Highway, Suite 1204, Arlington, VA 22202-4302. Respondents should be aware that notwithstanding any other provision of law, no person shall be subject to any penalty for failing to comply with a collection of information if it does not display a currently valid OMB control number. <b>PLEASE DO NOT RETURN YOUR FORM TO THE ABOVE ADDRESS.</b>					
1. REPORT DATE (DD-MM-YYYY) 05-18-2015		2. REPORT TYPE		3. DATES COVERED (From - To)	
4. TITLE AND SUBTITLE An Exploration of Structures in the Transitional Odd-Odd Nucleus Lu-160				5a. CONTRACT NUMBER	
				5b. GRANT NUMBER	
				5c. PROGRAM ELEMENT NUMBER	
6. AUTHOR(S) Hallgren, Steven Tyler				5d. PROJECT NUMBER	
				5e. TASK NUMBER	
				5f. WORK UNIT NUMBER	
7. PERFORMING ORGANIZATION NAME(S) AND ADDRESS(ES)				8. PERFORMING ORGANIZATION REPORT NUMBER	
9. SPONSORING / MONITORING AGENCY NAME(S) AND ADDRESS(ES) U.S. Naval Academy Annapolis, MD 21402				10. SPONSOR/MONITOR'S ACRONYM(S)	
				11. SPONSOR/MONITOR'S REPORT NUMBER(S) Trident Scholar Report no. 434 (2015)	
12. DISTRIBUTION / AVAILABILITY STATEMENT  This document has been approved for public release; its distribution is UNLIMITED.					
13. SUPPLEMENTARY NOTES					
14. ABSTRACT <p>Contrary to popular belief, not all nuclei are spherical. Past studies have determined that shells fill at certain “magic numbers” of nucleons when either the proton number (Z) or the neutron number (N) of the nucleus is, among other values, 82. The farther away a nucleus' Z or N is from these magic numbers, the more deformed it will be. Lutetium has 71 protons (Z = 71). A wide variety of isotopes of lutetium exist, which have the same Z but different N. As such, the transition between generally spherical lutetium nuclei and generally non-spherical nuclei occurs between N = 86 and N = 90, where Lu-160 (N = 89) lies.</p> <p>This project aimed to investigate the structure of such a transitional nucleus. The study required creating rapidly-spinning Lu-160 nuclei by means of a particle accelerator at Argonne National Laboratory. Once excited, an instrument called Gammasphere was employed to capture information about the high-energy photons. Experimental evidence showed abnormal signature splitting behavior in Lu-160. We believe this behavior is due to an alignment gain in Lu-160 that is hidden in its more rigid neighbors. The transitional nature of Lu-160 leaves it more susceptible to shape-driving effects of given nucleons, and allows for the additional malleability required to manifest this alignment gain which influences the nucleus' signature splitting.</p>					
15. SUBJECT TERMS Gammasphere, lutetium-160, signature inversion, triaxial					
16. SECURITY CLASSIFICATION OF:			17. LIMITATION OF ABSTRACT	18. NUMBER OF PAGES  68	19a. NAME OF RESPONSIBLE PERSON
a. REPORT	b. ABSTRACT	c. THIS PAGE			19b. TELEPHONE NUMBER (include area code)

# An Exploration of Structures in the Transitional Odd-Odd Nucleus $^{160}\text{Lu}$

Steven T. Hallgren  
Adviser: Professor Daryl J. Hartley

Trident Scholar Final Project Report  
Spring 2015

## Contents

<b>1</b>	<b>Introduction</b>	<b>3</b>
<b>2</b>	<b>Experimental Methods</b>	<b>4</b>
2.1	Function of LINACs . . . . .	4
2.2	Function of Gamma Ray Detectors . . . . .	5
2.2.1	Gamma-Ray Interactions with Matter . . . . .	5
2.2.2	Gamma Ray Detectors . . . . .	8
2.3	Compton Suppression . . . . .	9
<b>3</b>	<b>Nuclear Structure</b>	<b>11</b>
3.1	Nuclear Shell Model . . . . .	11
3.1.1	Shell Model Potential . . . . .	12
3.1.2	Shell Model Quantum Numbers . . . . .	14
3.2	Deformed Shell Model (Nilsson Model) . . . . .	15
3.2.1	Deformation Parameters . . . . .	17
3.2.2	Nilsson Quantum Numbers . . . . .	22
3.3	Pairing Effects . . . . .	23
3.4	Cranked Shell Model . . . . .	25
3.4.1	CSM Quantum Numbers . . . . .	26
3.4.2	Coriolis Effects . . . . .	27
3.4.3	Band Crossings . . . . .	30
<b>4</b>	<b>Experiment</b>	<b>32</b>
<b>5</b>	<b>Data Processing</b>	<b>34</b>
5.1	Detector Calibration . . . . .	34
5.2	Efficiency Correction . . . . .	35

5.3	Doppler Correction . . . . .	36
<b>6</b>	<b>Level Scheme</b>	<b>39</b>
6.1	Level Scheme Theory . . . . .	39
6.2	Level Scheme of $^{160}\text{Lu}$ . . . . .	43
<b>7</b>	<b>B(M1)/B(E2) Ratios</b>	<b>46</b>
7.1	Theory . . . . .	46
7.2	Experimental Data . . . . .	46
7.3	Theoretical Calculations . . . . .	47
<b>8</b>	<b>Signature Splitting and Inversion</b>	<b>54</b>
8.1	Signature Splitting . . . . .	54
8.2	Signature Inversion . . . . .	54
8.3	Signature Inversion Theory . . . . .	55
8.4	Experimental Data . . . . .	55
8.4.1	Trends within chains of isotopes . . . . .	57
8.4.2	Trends within chains of isotones . . . . .	57
8.4.3	Decrease of signature splitting magnitude . . . . .	58
8.5	Exceptions to the trends . . . . .	58
<b>9</b>	<b>Description of <math>^{160}\text{Lu}</math></b>	<b>60</b>
9.1	Alignment Gain and EF Transition . . . . .	60
9.2	Shape-Driving Effects of the EF Crossing . . . . .	62
<b>10</b>	<b>Conclusion</b>	<b>64</b>

## List of Figures

1	Sketch of a niobium drift tube . . . . .	4
2	The electromagnetic spectrum . . . . .	5
3	The photoelectric effect . . . . .	6
4	Compton scattering . . . . .	7
5	Cross sections for gamma-ray interactions with germanium . . . . .	8
6	Semiconductor band gap . . . . .	9
7	Woods-Saxon potential. . . . .	13
8	Shell model energy levels . . . . .	15
9	Deformed nucleus . . . . .	16
10	Ellipsoid cross section . . . . .	18
11	The Lund Convention for nuclear deformations . . . . .	21
12	Deformation classification . . . . .	21
13	$\Omega$ splitting in the $1d_{5/2}$ orbital . . . . .	22
14	Quasiparticle energy levels . . . . .	25
15	Coriolis effect in time-reversed orbits . . . . .	28

16	$^{162}\text{Hf}$ alignment . . . . .	29
17	Quasineutron energies of $^{162}\text{Hf}$ . . . . .	30
18	Heavy-ion reaction . . . . .	33
19	Detector calibration with $^{152}\text{Eu}$ . . . . .	34
20	Relative efficiency plot . . . . .	35
21	Doppler effect in Gammasphere data . . . . .	37
22	Measurement of $\beta$ in reaction . . . . .	38
23	Excerpt of the level scheme for $^{161}\text{Lu}$ . . . . .	40
24	Sample process of taking gates . . . . .	42
25	Example spectrum of $^{160}\text{Lu}$ . . . . .	43
26	Proposed level scheme for $^{160}\text{Lu}$ . . . . .	45
27	$^{160}\text{Lu}$ branching ratios . . . . .	48
28	Nilsson diagram for protons . . . . .	49
29	Nilsson diagram for neutrons . . . . .	50
30	Signature splitting systematics for $A \approx 160$ nuclei . . . . .	56
31	Alignment plots for $N = 89$ nuclei . . . . .	61
32	Alignment plots for bands in $^{162}\text{Hf}$ . . . . .	62
33	Shape-driving effects of nucleons . . . . .	63

## Abstract

Though it is commonly believed that all nuclei are spherical, they in fact come in a variety of shapes depending primarily upon how many protons and neutrons they have. The principle method used to investigate the shape of the nucleus is exciting it to high angular momentum and observing the gamma rays emitted as the nucleus slows down. Based on characteristics and patterns of these emissions, we can discern the structure of the nucleus and which specific nucleons contribute to that structure.

From observational evidence, it is known that nuclei tend to be spherical when they have close to a “full shell” of nucleons. This concept is similar to the stability of noble gases caused by full shells of electrons. Past studies have determined that shells fill at certain “magic numbers” of nucleons, when either the proton number ( $Z$ ) or the neutron number ( $N$ ) of the nucleus is, among other values, 82. The farther away  $Z$  or  $N$  is from these magic numbers, the more deformed the nucleus will be.

Lutetium has 71 protons ( $Z = 71$ ), though there are a wide variety of lutetium isotopes all with the same  $Z$  but different  $N$ . It is possible to observe an evolution in deformation as  $N$  is increased.  $^{157}\text{Lu}$  is still nearly spherical even with 86 neutrons, 4 beyond the magic number of 82. However, at  $N = 90$  ( $^{161}\text{Lu}$ ), the nucleus becomes well-deformed and exhibits very few properties of a spherical nucleus. As such, the transition between generally spherical lutetium nuclei and generally non-spherical nuclei occurs between  $N = 86$  and  $N = 90$ , where  $^{160}\text{Lu}$  ( $N = 89$ ) lies.

This project aimed to investigate the structure of such a transitional nucleus, identify the predominant factors influencing its shape, and explore signature splitting in the atomic mass ( $A \approx 160$ ) region. High-spin states of  $^{160}\text{Lu}$  were populated using the  $^{120}\text{Sn}(^{45}\text{Sc}, 5n)^{160}\text{Lu}$  reaction at Argonne National Laboratory. The reaction ran at a beam energy of 215 MeV for a total of 3 days of data collection.

An instrument called Gammasphere was employed to capture information about the high-energy photons (gamma rays) that these excited states emit as they cool. Gammasphere houses up to 110 high-purity germanium, Compton-suppressed gamma ray detectors. The device is particularly well-suited for the study of very faint rotational sequences and observing the highest spins of rotational bands.

Experimental evidence showed abnormal signature splitting behavior in  $^{160}\text{Lu}$ . We believe this behavior is due to an alignment gain in  $^{160}\text{Lu}$  that is hidden in its more rigid neighbors. The transitional nature of  $^{160}\text{Lu}$  leaves it more susceptible to shape-driving effects of given nucleons, and allows for the additional malleability required to manifest this alignment gain which influences the nucleus’ signature splitting.

Keywords: Gammasphere,  $^{160}\text{Lu}$ , signature inversion, triaxial

## Acknowledgments

Sitting down to write this portion implies that I have run out of edits to make to the ensuing pages which is a position I could hardly imagine myself in at the outset of the project. I somehow managed to reach the point that this too-thick report is in your hands, and it certainly was not by myself. I could not begin to rank the help I received in order of importance, so instead I will move chronologically.

The first thanks goes to my parents Eric and Cheryl for laying the foundation on which I continue to build. You managed to teach me to value education and self-improvement in a way that I am certain I would never have learned on my own. The fact that I know you both will read every word of this report despite it being, I quote, “all  $E = mc^2$  to [you]” means a lot to me.

A number of my high school teachers impacted me tremendously in ways I feel even today. Thanks to Mrs. Christine Baker for teaching me how to write and to loathe the passive voice. One day the world may see a scientist who can also write well, and I am sure that person will have taken English from you. Mr. Rob Bass and Mr. Mike McCormack instilled in me the love of math and science that lead me down this path. I can only hope to be able to communicate science as effectively and charismatically as you did. Finally, I want to thank Mr. Darren Gabrielsen for mentoring me and teaching me everything else I did not know I needed to know.

Brandon Karpf, my close friend and perpetual roommate, deserves my endless gratitude for letting me keep the light on late at night and for pretending to have any idea what I was working on all year. I wish you the best of luck at M.I.T. though we both know your grades will suffer without me.

Thanks to Dr. Dan Isaac for the wealth of advice, expertise, and support over the years. I will always look to you as the epitome of what it means to truly care about those in my charge. I’d also like to thank Dr. Christopher Morgan for writing me an endless slew of recommendations and for providing a uniquely Navy perspective on Academia.

Last, but perhaps most significantly of all, my sincerest thanks go to my research adviser, Dr. Daryl Hartley, though “thanks” at times seems like too inadequate a word. I learned an incredible amount over the last two years not only about nuclear physics, but also about all the intangibles like navigating the politics of science and how bureaucracy will not end with a return to civilian life. I owe such a vast portion of my success to your unyielding willingness to bend over backwards for me and your unwavering patience even as you explained what alignment was for what must have been the three hundredth time.

To the members of the Trident Committee with twelve more of these reports to read, I appreciate your diligence and hope that your endeavor is paper cut-free. For anyone else preparing to delve into this report, I cannot promise that you will find it as interesting to read as I found it to write, though I do hope you learn something along the way.



# 1 Introduction

At the beginning of this project, we intended to study two exotic phenomena that occur in high-spin nuclei. Both phenomena imply the existence of an asymmetrically-shaped nucleus, where one of the phenomena, known as “wobbling,” is a product of spinning something like an asymmetric top [1]. The other phenomenon, ultra-high spin bands, is only seen at the upper limits of angular momentum [2]. These phenomena have only been seen in isolation in individual nuclei. There is good reason to believe that if these phenomena could simultaneously appear in the same nucleus, they would most likely be linked together in  $^{161}\text{Lu}$ . However, scheduling and technical problems at Argonne National Laboratory, where the experiment was to be run, prevented the collection of the data in a timely manner to complete the intended project.

Fortunately, a trial reaction was run in the process of testing equipment upgrades at the lab, where the same reaction we had intended to use for the study of  $^{161}\text{Lu}$  was performed. However, for the purposes of this project, the data that the trial reaction yielded was not optimized for our study due to three primary factors. For one, the trial run was 40% shorter than the intended experiment. The trial consists of only three days of data collection, vice the five days we have scheduled. Second, there were 15% fewer detectors online than normal. Finally, only 1/3 of the total beam intensity was achieved. The structures and patterns that we hoped to identify in  $^{161}\text{Lu}$  are expected to be so faint that they would only be visible in analyzing larger amounts of data than the trial could provide. However, the trial data set did provide a significant amount of new information concerning the odd-odd nucleus  $^{160}\text{Lu}$  (meaning that it has an odd number of both protons and neutrons).

Roughly one-third of nuclei are spherical or near-spherical, particularly those near magic shell gaps of stability. These magic gaps represent full nuclear shells in much the same way that the filling of electron shells gives noble gases their stability. A shell of the nucleus becomes full when it reaches a point where the binding energy of adding one more nucleon is greater than the binding energy it took to add the last nucleon. As such, full nuclear shells represent particularly stable configurations of the nucleus in that adding additional nucleons requires a great amount of energy. From both experimental and theoretical evidence, the magic gaps are canonically held to be located at either proton number ( $Z$ ) or neutron number ( $N$ ) equal to 2, 8, 20, 28, 50, 82, or 126. As nuclei move away from filled magic shell gaps, they tend to become more and more deformed.

Focusing on isotopes of lutetium (in other words, keeping  $Z$  fixed at 71), it is possible to observe an evolution in deformation as  $N$  is increased. Even with as many as 86 neutrons, 4 beyond the magic number of 82,  $^{157}\text{Lu}$  is still just barely deformed away from a spherical shape. However, at  $N = 90$  ( $^{161}\text{Lu}$ ), the nucleus becomes well-deformed and exhibits very few properties of a spherical nucleus. As such, the transition between generally spherical lutetium nuclei and generally non-spherical lutetium nuclei occurs between  $N = 86$  and  $N = 90$ , where  $^{160}\text{Lu}$  ( $N = 89$ ) lies. In fact, triaxial deformation (which describes an asymmetrically-shaped nucleus) is thought to play a pivotal role in this transitional region. Thus, an analysis of the structures of this nucleus will provide insight into the transitional regime of deforming nuclei.

## 2 Experimental Methods

### 2.1 Function of LINACs

A tremendous amount of excitation energy is required to populate the nuclear states of interest in this project. The reaction we ran requires sufficient energy to overpower the repulsive electromagnetic Coulomb forces that would otherwise prevent the nuclei from coming into contact. The prerequisite energy can be obtained by accelerating a nucleus through a particle accelerator.

The accelerator utilized for this work is ATLAS (Argonne Linear Accelerator System) located at Argonne National Lab. ATLAS, as its name implies, is a linear accelerator (LINAC) capable of reaching energies of 7-17 MeV/nucleon [3]. Broadly speaking, LINACs utilize pulsed radio-frequency (RF) waves to accelerate particles down a wave guide towards a target at the opposite end. Doing so requires a substantial amount of engineering precision in terms of the timings and tolerances necessary to achieve effective acceleration. Though many facilities can achieve vastly higher energies, the types of reactions of interest to those studying nuclear structure tend to need energies close to, but not greater than, the Coulomb barrier of the nucleus.

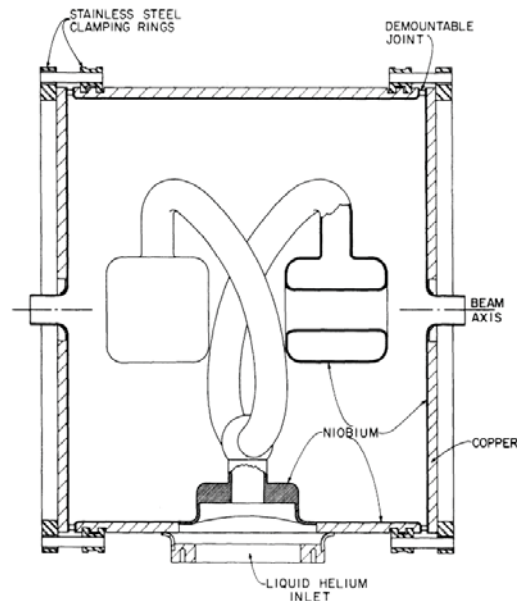


Figure 1: Sketch of a niobium drift tube as employed in the ATLAS facility [6].

LINACs alternately attract and repel the charged beam particle along the length of the tube. This is accomplished by a series of niobium “drift tubes” that are each split in half (Figure 1). However, since the beam particles begin as neutral elements, they must first be stripped of some of their outer electrons to acquire a net positive charge. Then, each drift tube is charged with the opposite charge on each half of the tube. Thus, the beam is attracted to the front side of the next tube and repelled from the back side of the tube that it just left. As the beam passes into the middle of the drift tube, the polarization of the tube must be reversed in order to continue its acceleration. In order to maximize the acceleration effect, the polarity needs to be changed as rapidly as possible.

To facilitate the rapid polarity changes, each drift tube is cooled until it becomes superconducting (at approximately 9 K for niobium [4]). This helps maximize the energy transfer and minimize losses that would occur at higher temperatures. Otherwise, it would be impossible to alternate the charge rapidly enough to effectively accelerate the beam. As the beam is accelerating, a variety of electric and magnetic fields steer it along its path and collimate it down to the desired size. Finally, at the end of the accelerator, the beam is directed at target material that is housed in one of several experimental devices. In the case of this project, the device was a suite of gamma-ray detectors known as Gammasphere [5] which was utilized to detect the emissions of the collision.

## 2.2 Function of Gamma Ray Detectors

### 2.2.1 Gamma-Ray Interactions with Matter

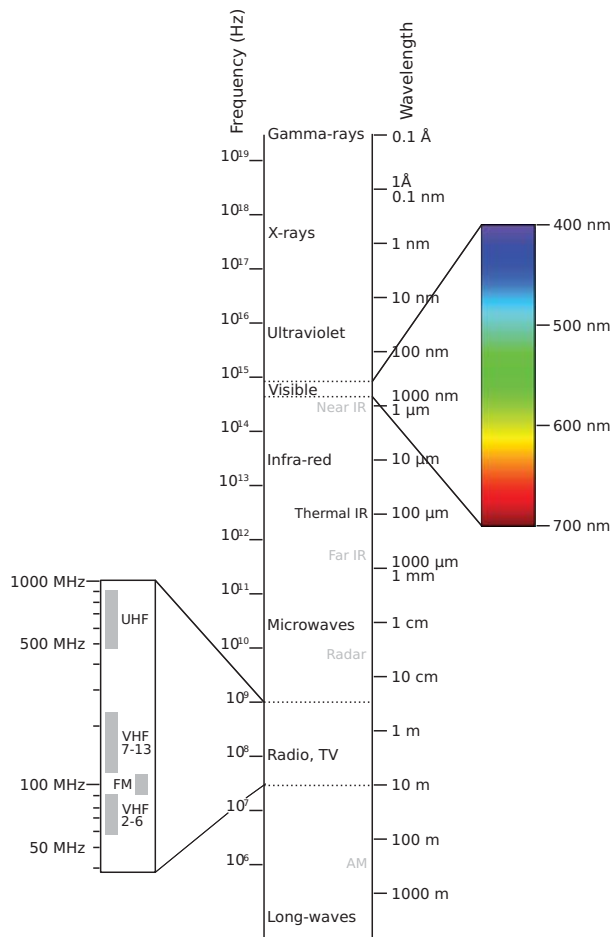


Figure 2: Graphical representation of the various types of radiation that comprise the electromagnetic spectrum [8].

Before discussing how we can collect information on gamma rays, our first approach to the problem should be to gain an understanding of how gamma rays interact with matter. After all, it will be through exploiting these interactions that we will be able to discern more quantitative information about the gamma rays themselves.

Gamma rays are simply a form of electromagnetic (EM) radiation, just like light. However, gamma rays comprise the portion of the EM spectrum distinguished by having extraordinarily high frequencies, and consequently very short wavelengths (Figure 2). This implies that gamma rays represent the most energetic side of the EM spectrum. Planck's equation explicitly reveals the direct proportionality between energy and frequency:

$$E = hf \quad (1)$$

where  $E$  is energy,  $h$  is Planck's constant of proportionality, and  $f$  is the frequency. Thus, gamma rays follow many of the same basic principles of behavior that we are accustomed to seeing in visible light. However, their significantly higher energy yields interesting new effects. Since gamma rays fall at the highest energy end of the EM spectrum, they do not

have an upper boundary on their energy and so their interactions can be broken into three general

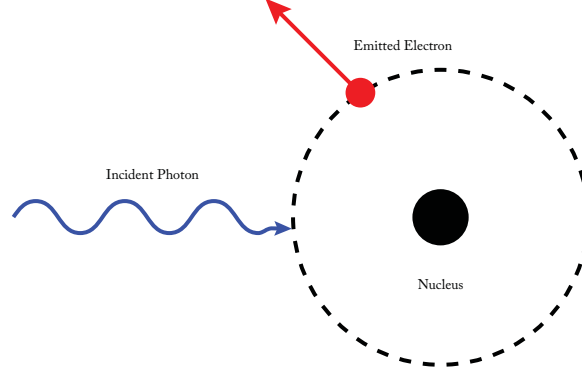


Figure 3: A diagram of a typical photoelectric absorption and emission event.

categories depending on the energy of the gamma ray in question. In general, the unit of energy employed when discussing gamma rays is the electron volt (eV).  $1 \text{ eV} = 1.6 \times 10^{-19} \text{ J}$  and is the energy required to move a single electron across an electrical potential difference of 1 V. The majority of the following information comes from reference [7] with supplemental sources provided as needed.

**Photoelectric Absorption** ( $< 100 \text{ keV}$ ) Also known as the photoelectric effect, this phenomenon was utilized as early experimental evidence that energy was quantized into discrete bundles and was not a continuous quantity. In fact, despite the rest of the dramatic and revolutionary 20th-Century developments that followed, an accurate description of the photoelectric effect was the only discovery that won Albert Einstein a Nobel Prize [9].

The photoelectric effect occurs when atoms absorb relatively low-energy gamma rays and then release this energy through the emission of an electron. The energy exchanged during such a reaction is given by:

$$T_e = E_\gamma - \phi \quad (2)$$

where  $T_e$  is the kinetic energy of the emitted electron,  $E_\gamma$  is the energy of the gamma ray, and  $\phi$  is the *work function* of the absorbing atom, which represents the amount of energy needed to eject an electron. Figure 3 shows a representation of the photoelectric effect. Empirically, we know that the probability of the photoelectric effect occurring is tremendously dependent on  $E_\gamma$ , dropping off significantly as  $E_\gamma$  increases. Only the lowest energy gamma rays seen in our experiments will interact through this mechanism, though it is convenient when they do as the entirety of  $E_\gamma$  will be deposited into the absorbing atom.

**Compton Scattering** (100 keV– 1 MeV) If a gamma ray impacts an atom with too much energy to be directly absorbed, it will instead scatter in a different direction while simultaneously ejecting an electron from the atom. This process is known as Compton scattering and is shown in Figure 4. For the most part, the energies associated with electrons in an atom's orbital are far less than  $E_\gamma$  when Compton scattering occurs, so we can treat the electron as if it is at rest and the collision as

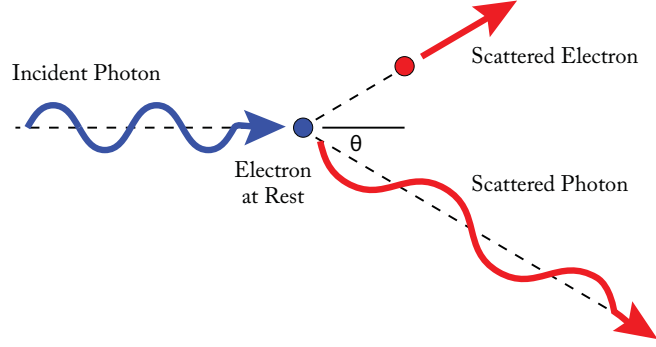


Figure 4: A diagram of Compton scattering. Adapted from [10].

if it were elastic [11]. As such, the leftover energy in the scattered gamma ray ( $E'_\gamma$ ) is a function of its original energy ( $E_\gamma$ ) and the angle it was scattered at:

$$\cos \theta = 1 - m_e c^2 \left( \frac{1}{E'_\gamma} - \frac{1}{E_\gamma} \right) \quad (3)$$

where  $m_e$  is the mass of an electron and  $c$  is the speed of light. Of course,  $0^\circ \leq \theta \leq 180^\circ$  which allows for a wide variety of deposited energies. However, there is a maximum energy corresponding to  $\theta = 180^\circ$ . This energy is known as the *Compton edge* since it is impossible for the gamma ray to transfer any more energy in a Compton scattering event than this value. The Compton edge is given by:

$$E_{\text{edge}} = \frac{2(E_\gamma)^2}{m_e c^2 + 2E_\gamma} \quad (4)$$

Gamma rays can scatter an indefinite number of times with the hopeful end result of eventually being photoabsorbed inside the detector. However, as we will see later, we frequently are not so lucky. The energies from which Compton scattering is most often observed are precisely the energies of interest in our study so we must carefully consider such effects.

**Pair Production ( $> 1.022 \text{ MeV}$ )** The final potential interaction is known as pair production. Per the infamous equation  $E = mc^2$ , mass can be converted into energy and vice-versa. So long as momentum and charge are conserved, gamma rays with sufficient energy can spontaneously create an electron-positron pair. This requisite energy is  $1.022 \text{ MeV} = 2m_e c^2$  and is much greater than what will typically be encountered in a high-spin emission from the nucleus.

Figure 5 shows the different types of gamma-ray interactions with matter and the energy regimes in which they are dominant.

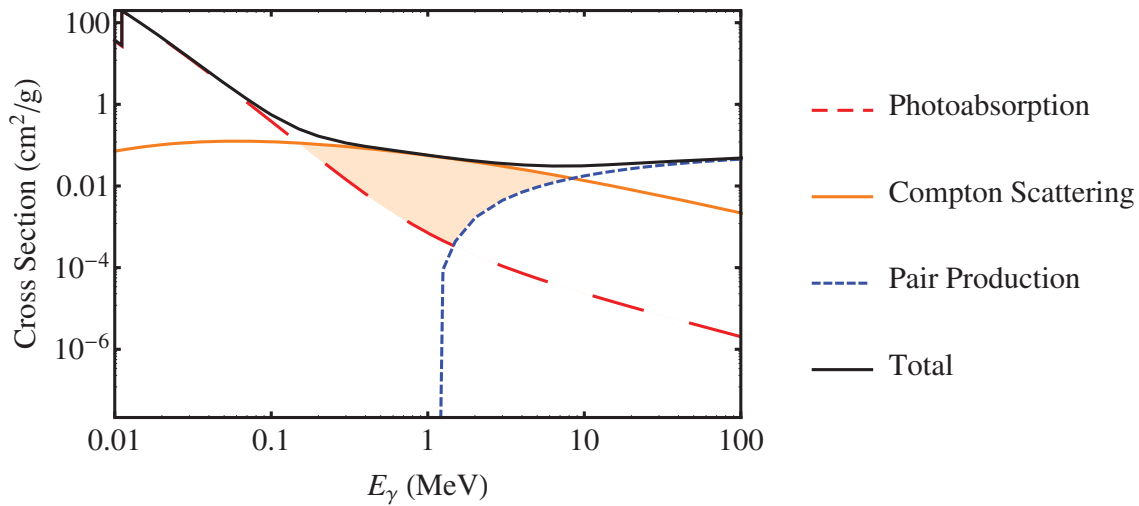


Figure 5: Cross sections (equivalent to probability) for various gamma-ray interactions with germanium. The shaded region denotes the range of energies for which Compton scattering is the most prevalent effect. Data taken from [12].

### 2.2.2 Gamma Ray Detectors

In order to collect data on how  $^{160}\text{Lu}$  nuclei decay, it is necessary to develop a method of collecting the gamma rays emitted during this decay process. The chosen tool for this task is a high-purity germanium (HPGe) semiconductor detector. Although there are numerous different tools that can detect gamma rays, semiconducting devices are preferred for their high energy resolution—that is, the ability to distinguish energies of gamma rays that are very close in energy to each other. This property is critically important to the study of nuclear structures as the gamma rays that distinguish different decay bands may differ by just 1 or 2 keV.

Semiconducting elements are those that have properties somewhere in between those of a pure conductor and those of a pure insulator. Germanium, along with other elements on the border between halogens and metals (notably silicon), has such properties. The valence shell of germanium has four electrons, filling it half-way. Because it has these four electrons to form covalent bonds, it tends to form a regular crystal lattice structure by bonding with its four nearest neighbors. In this state, all electrons are fixed in place in the structure of the lattice.

The basic property of metals that allow them to conduct electricity well is that their valence electrons are *delocalized*, meaning that they are not fixed to a single atom but rather are free to move from atom to atom throughout the entire solid lattice. The electrons in the ground state of an atom (that is, an atom with no added energy) are said to exist in the *valence band* of that element. In order for the electrons to become mobilized as they are in metals, they must receive enough additional energy to break out of the valence band and enter the *conduction band* of that material (See figure 6). To do so, they must receive at least enough energy to cross the band gap, which is a region of energies where the electrons cannot exist. For metals and other conductors, the valence band and conduction band overlap, meaning that electrons are always delocalized while

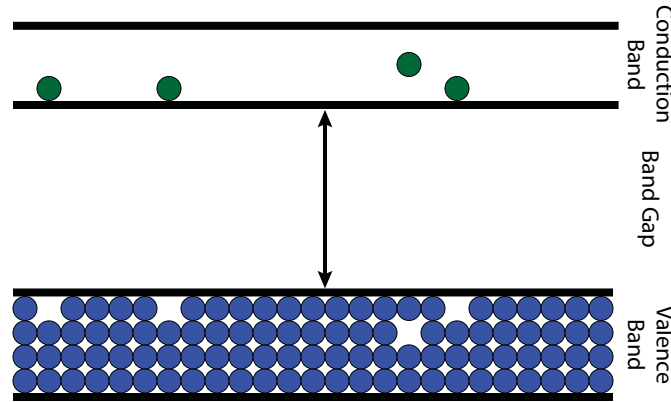


Figure 6: Band gap structure of a typical semiconductor. Adapted from [13].

under typical operating conditions. For others, the electrons first must be excited to cross the band gap. Insulators typically require  $\approx 6$  eV to cross the band gap. Semiconductors mediate these two extremes as their band gap energies are typically small ( $\approx 1$  eV), allowing the material to readily conduct electricity after receiving a small amount of energy. For instance, germanium's band gap is approximately 0.72 eV [14]. Although this technically does place a lower limit on the energies of photons that HPGe can detect, even the lowest energy gammas produced from the decay of a nucleus are on the order of hundreds of keV and, as such, much greater than germanium's band gap.

The operating principle of semiconductor detectors is that incoming gamma rays provide the electrons in the semiconducting crystal with a certain amount of energy which excites a given number of electrons into the conduction band. When the electrons leave the valence band, they create a net-positively charged “gap” which is called an *electron hole*. When a significant voltage is applied to the semiconductor, the electrons move to one contact and the holes move to the other (in the sense that the rest of the electrons “shift over,” thereby moving the hole to one side), producing a potential difference. Figure 6 illustrates the energy spacing between the valence band and the conduction band, as well as a few electrons that have been excited into the conduction band. Because the band gap energy for different kinds of semiconductors is known, the magnitude of the potential difference can be used to determine how many electron-hole pairs were formed, and consequently the energy of the original gamma ray.

## 2.3 Compton Suppression

Ideally, the germanium atoms would absorb the entirety of the energy of gamma rays all at once. However, since the gamma rays we are interested in studying are within the range of Compton scattering dominance, we know that this is unlikely. After a single scattering event, the gamma has lost some energy, some electron-hole pairs have been produced, and the photon is now traveling in a different direction. If the photon remains in the germanium crystal such that it continues to interact with other germanium atoms until it is entirely absorbed, no error is introduced. The net sum of electron-hole pairs is the same as it would be if all of the energy was absorbed at once, not to mention the fact that the time scale even for numerous scattering events is too small to detect.



However, a problem does arise if the photon is scattered in a direction that sends it out of the crystal at any time before its energy is entirely absorbed. When this happens, an incorrect energy will be recorded thus adding noise, known as *Compton background*, to the experimental data.

To combat the Compton background, a technique known as Compton suppression has been developed to limit noise. Compton suppression involves surrounding the HPGe detector with another detector to look for any gammas that are scattered out of the germanium. In this case, the other detector is a Bismuth-Germanate (BGO) scintillator detector. A scintillator works essentially like a semiconductor detector does, except that rather than using delocalized electrons to produce an electric pulse, it produces a pulse by using de-exciting electrons that produce photons after striking a photosensitive plate. The photons are then amplified by photomultiplier tubes and then converted to an electric pulse. In general, scintillators have much lower energy resolution than do semiconductor detectors, but the energy resolution of the BGO detector is irrelevant for Compton Suppression as the BGO is employed to remove extraneous data rather than to try to recover it. BGO is roughly 34% more dense than Ge, so it is safe to assume that any photons that enter the BGO detector will stop there and be absorbed.

Both the HPGe and the BGO detectors are run simultaneously while experimental data is collected. When the experiment is running, gamma rays that occur within the same coincidence window of both detectors are identified and electronically vetoed, meaning that they never enter the data set. If both detectors witness an event at the same time, that gamma must have been scattered out of the HPGe detector before its energy was fully absorbed. By canceling such an event, fewer partial energies will be recorded by the main detector. As a result, the background noise of the data set is greatly reduced allowing weaker gammas to be discerned than could have been otherwise.

Ideally, it would be best to surround a reaction completely with HPGe detectors, but there are immediate logistical constraints as larger germanium detectors become prohibitively expensive and also lose energy resolution. One factor contributing to the increased resolution of small detectors is the lesser degree to which the Doppler effect alters photon energies. The Doppler effect is a change in the observed frequency of a wave depending on the source of the wave's relative motion with respect to the detector of the wave. Although the Doppler effect is often discussed in the context of sound waves, a gamma ray is just another variety of wave. Individual gamma rays are referenced by their energy, but, as in Equation 1, the frequency of the gamma ray can also be influenced by Doppler shifts.

In this case, the moving source is the nucleus produced in the heavy-ion reaction. As the compound nucleus will not be stationary after the reaction, the gamma ray is emitted by a source that is moving and, therefore, the frequency (and more importantly, the energy) of that gamma ray will be influenced by the direction from which the gamma ray is observed. If the detector was very large, different areas of the crystal surface could see different Doppler shifts depending on the incidence angle of the gamma. By using smaller detectors, the change in Doppler shift from one side of the detector to the other is minimal, allowing for a better measurement of the original intensity. Considering the effects of Doppler shifts was critical to the analysis of our experimental data, and will be discussed further in section 5.3.



### 3 Nuclear Structure

Before presenting our experimental results, we would be remiss not to provide a rough sketch of the theory of nuclear structure we employed in our analysis. This section provides a foundation in much of the terminology and theory utilized in the presentation of our data.

Ultimately, the goal of nuclear physics is to develop a model for the behavior of the nucleus in general. In other words, to create a way of thinking about nuclei both physically and mathematically that *explains* all of the unique characteristics of every known nucleus and *predicts* characteristics of nuclei not yet observed. Unfortunately, there is no such unified model of nuclear physics. There are, however, a wide variety of isolated models utilized for mathematical calculations and physical descriptions of specific behaviors in specific nuclei. Even still, many of these models excel in the regimes they are tailored to fit. Because experimental results corroborate theoretical predictions using these models, we can confidently proceed with the cautioned understanding that such a model has some basis in physical reality, albeit perhaps an imperfect one. Variants of the nuclear shell model serve our purposes well for our work in the  $A \approx 160$  region.

#### 3.1 Nuclear Shell Model

By way of introduction to the shell model, it is perhaps best to illustrate it through its chemistry analog: the atomic shell model. In truth, much of the notation and nomenclature for the nuclear shell model was borrowed from chemists since this analogy works so well.

The atomic shell model holds that, in an atom, the electrons “orbit” within the electromagnetic potential created by the central force of the Coulomb attraction of the nucleus. The electrons exist in *orbitals* as defined by their quantum numbers. As additional electrons are added into the atom, they are placed in successively higher shells, typically referred to as *energy levels*. However, the handy trick of the shell model is that, when studying the properties of any given atom, it is unnecessary to consider every particle in every shell. Rather, we only need consider the outermost shell, the *valence shell*, of electrons which governs the properties of that atom.

The impetus behind the creation of a shell model for the nucleus came out of a desire to explain the patterns of stable nuclei. Well before the development of this model, researchers observed that nuclei with particular numbers of nucleons ( $Z$  and/or  $N$  equal to 2, 8, 20, 28, 50, 82, or 126) had unusually high binding energies per nucleon than what would be expected based on theoretical calculations and the behavior of neighboring nuclei. Binding energy represents the amount of energy needed to break apart the nucleons, so these higher values represented abnormally stable nuclei. An elegant explanation of these numbers, referred to as the magic numbers, became the primary focus of theoretical nuclear physicists.

Atoms exhibit similar behavior. As one moves left-to-right across the periodic table, certain properties of the atoms gradually change up to the noble gases. Upon wrapping around the table, there is a dramatic change in behavior before a similarly gradual trend emerges again. Clearly, a significant phenomenon occurs between the noble gases and the alkali metals on the ends of the periodic table. Early atomic chemists described this phenomenon as the filling of atomic shells with elec-

trons. As the shells become completely filled, they exhibit great stability (the noble gases). Since the atomic shell model succinctly described the stability and behavior of atoms, it was thought that a similar approach could also explain the magic numbers in nuclei.

This same basic framework very roughly summarizes the nuclear shell model, with a few key difficulties of translation. For one, an orbit requires a potential of some sort. Atomically, this is fairly simple as the electrons orbit the fixed potential created by the nucleus. Moreover, due to the relatively small size of the nucleus compared to the electron cloud, it is fairly easy to understand how the electrons could occupy “spatial” orbitals and physically orbit the nucleus without colliding. However, within the nucleus, we enter a recursive loop as the nucleons move about a potential that they themselves create. Similarly, the nucleons are so physically close together that it is difficult to imagine how they could occupy such spatial orbitals without colliding.

Just as the atomic shell model prevented us from having to consider all of the sub-shell electrons, the nuclear shell model allows us to consider each individual nucleon as it orbits the potential of the rest of the nucleons. This approximation dramatically reduces the mathematical complexity of the many-body problem that would otherwise govern interactions in the nucleus. The spatial orbits of the nucleons are resolved by the Pauli principle. As discussed below in Section 3.3, nucleons tend to pair in groups of two in their orbits about the nucleus. If they were to collide, the orbital angular momentum of the particle pair would transfer in the collision to attempt to excite the nucleons to a higher energy level. However, the lower energy levels within the nucleus are located “beneath” a large number of higher energy levels that are already filled. Since the Pauli principle prevents multiple pairs of nucleons from co-inhabiting the same orbital, the only opportunity for the supposedly colliding nucleons to promote in energy level would be to jump all the way up to the valence shell. For the vast majority of nucleons, especially in large  $A \approx 160$  nuclei, the energy gap between inner-shell nucleons and the valence shell is far greater than what could be expected to transfer in such a collision. Thus, since these collisions are greatly energetically disfavored, they do not occur and we can imagine that the nucleons do fill such spatial orbitals. That being said, the logical extension of that argument is that certain upper-shell nucleons *would* be able to collide since the energy difference is smaller. This effect does occur, and its importance to our work will be discussed in Section 3.3.

### 3.1.1 Shell Model Potential

**Woods-Saxon Potential** As mentioned previously, any model that includes spatial orbitals must also include some form of a potential about which the nucleons can orbit. The design of an appropriate potential is crucially important to the model’s ability to produce accurate results. Initial guesses attempted to reuse canonical quantum mechanical potentials, such as an infinite square well or a harmonic oscillator potential. The chief problem encountered while using these potentials is that they fundamentally do not reflect the reality of the potential generated by the nucleus, though they do make the calculations easier. Particles require an infinite amount of energy to escape from these potentials, though they naturally can actually escape with some finite amount of energy.

The initial refinement of the shell model potential was selecting a function that would smoothly

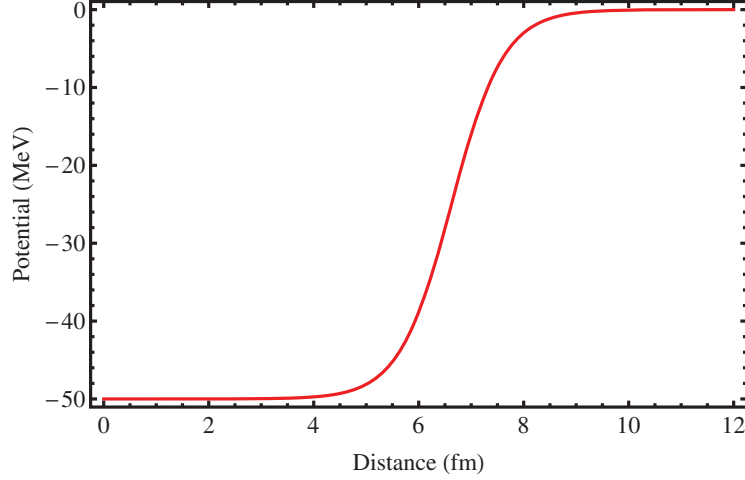


Figure 7: Woods-Saxon potential calculated for an  $A = 160$  nucleus. Parameters were  $V_0 = 50$  MeV,  $a = 0.5$  fm, and  $r_0 = 1.22A^{1/3}$  fm.

transition to zero with increasing distance from the nucleus. Such a potential is known as a Woods-Saxon potential and is preferred as it more accurately reflects the experimentally determined charge distribution of the nucleus. For a distance  $r$  away from the center of the nucleus, the potential is of the form [15]:

$$V(r) = -\frac{V_0}{1 + \exp\left(\frac{r-R}{a}\right)} \quad (5)$$

where  $V_0$  is a representation of the strength of the field,  $R$  is the radius of the nucleus and  $a$  is a diffuseness parameter. A sketch of this potential is shown in Figure 7.

Although the Woods-Saxon potential represented a significant improvement on previous potentials used for shell model calculations, it still did not entirely reproduce the observed magic numbers. Some further modification was needed to better fit reality.

**Spin-Orbit Potential** It was eventually discovered that the missing component of the shell model potential is a spin-orbit interaction of the nucleon. This concept is derived from the much more fully developed idea of atomic spin-orbit interactions, where the intrinsic spin of the electrons creates a magnetic moment that interacts with the magnetic field generated from the apparent orbital motion of the nucleus about the electron. The underlying physical explanation of the nuclear spin-orbit interaction is still not entirely understood, though adopting the form and concept of such a potential from atomic physics reproduces the magic numbers. Thus, there is some basis for the existence of this potential in reality.

The angular momentum due to the nucleon's orbit is referred to as  $\ell$  and the intrinsic spin of the nucleon is referred to as  $s$ . Accordingly, for a given nucleon, we can define a quantity called the total angular momentum as the vector sum  $\mathbf{j} = \ell + \mathbf{s}$ .  $s$  can either be aligned parallel or anti-parallel to  $\ell$ , yielding splitting of the total angular momentum as  $j = \ell \pm \frac{1}{2}$  since, for a single nucleon,

$|\mathbf{s}| = \frac{1}{2}$ . It is the consideration of the orientation of this alignment that provides the potential the necessary complexity to explain observed experimental results.

The directional orientation of the spin-orbit interaction is attached to the overall potential as a dot product [7]:

$$V(r) = V_{\text{so}}(r)\ell \cdot \mathbf{s} \quad (6)$$

The effective result of this new potential is that, for a given  $\ell$ , the orbital with an aligned spin term is much more tightly bound to the nucleus and lies at a substantially lower energy level than the anti-parallel orbital. The magnitude of this energy splitting depends on the magnitude of  $\ell$ :

$$\Delta E = \frac{1}{2}(2\ell + 1)\hbar^2 \quad (7)$$

At high  $\ell$ ,  $\Delta E$  is so large that the down-shifted orbital leaves its original shell and forms its own, lower-energy shell. The right portion of Figure 8 shows the splitting of the orbitals due to the spin-orbit potential. Note in particular the  $1f_{7/2}$  and  $1g_{9/2}$  orbitals that occupy the gaps in between shells. These gaps were essential in order to correctly explain the observed magic numbers. Critically, the actual orientation of the orbit of the nucleus is irrelevant leading to the  $2j + 1$  degeneracy observed in each state that reproduces the magic numbers.

### 3.1.2 Shell Model Quantum Numbers

When discussing quantum mechanics and specific states of a system, it is useful to have a discreet and consistent method of identifying the different states a nucleon can exist in. This labeling convention employs quantum numbers, much as with electrons, to uniquely identify states. However, not all of the atomic quantum numbers apply in the nuclear realm. The shell model employs the following four quantum numbers [16]:

1.  $n$  is the index of the orbital. Although this looks deceptively similar to the principal quantum number of chemistry, the first shell model quantum number is completely different. Though both refer to a sequential energy level of sorts, in the atomic realm,  $n$  represents the overall excitation and potential energy of the electron. In the nuclear realm, however,  $n$  is more of counter representing the first, second, third, ... orbital that has a particular  $\ell$ .
2.  $\ell$  is the orbital angular momentum of the state. The value of  $\ell$  matches to the traditional spectroscopic labels from chemistry, in that  $\ell = 0$  is an  $s$  orbital,  $\ell = 1$  is a  $p$  orbital,  $\ell = 2$  is a  $d$  orbital, and so forth.
3.  $j$  is the total angular momentum of the nucleon as described above.
4.  $m_j$  is the projection of  $j$  onto a specified axis, traditionally taken to be the  $z$  axis. Although the value of  $m_j$  has no physical effect in a spherical potential, it is important to consider in the degeneracy of a state with a given  $j$ . Since the angular momentum can be fully aligned

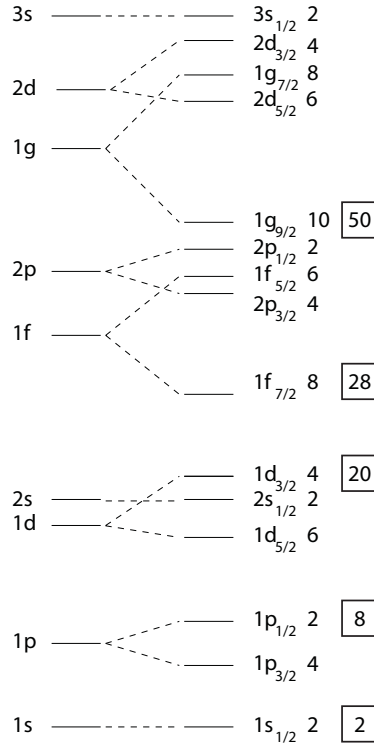


Figure 8: Energy levels of the nuclear shell model. The left side shows the degenerate shell model potential and the right shows the energy level splitting caused by the inclusion of the spin-orbit potential. The numbers next to each orbital indicate the degeneracy, or capacity of nucleons, of that orbital and the boxed numbers indicate where the magic numbers occur. Note that the down-shifting of the  $1f_{7/2}$  and  $1g_{9/2}$  orbitals allow for the occurrence of magic numbers in between shell gaps.

forward or back on that axis, and integer steps in between, a given  $n$ ,  $\ell$ , and  $j$  can have  $2j + 1$  values of  $m_j$  and consequently  $2j + 1$  nucleons.

### 3.2 Deformed Shell Model (Nilsson Model)

As successful as the shell model is at predicting the magic numbers, its foundation rests upon the fundamental assumption that the nucleus is spherical. Such a spherical nucleus creates a uniform, spherical potential. However, nuclei are only spherical insofar as their  $Z$  and  $N$  are near magic numbers. As seen in Figure 8, the first few magic numbers are relatively close together. Accordingly, nuclei in these regions are typically spherical because, even if they are in the middle of the mid-shell gap, they are not very far from the magic numbers.

As the magic numbers spread apart, specifically between 50 and 82 in the  $150 \leq A \leq 190$  region, nuclei that exist at mid-shell (halfway between gaps) are far enough away from the magic numbers that they are markedly deformed. Since nuclei in this region are the focus of our study, we require further modifications to our potential to more accurately represent the physical reality of the nuclei in this study. These modifications maintain the same basic premises of the regular shell model, but

allow for the decoupling of the motion of the nucleon about the nucleus from the motion of the nucleus itself.

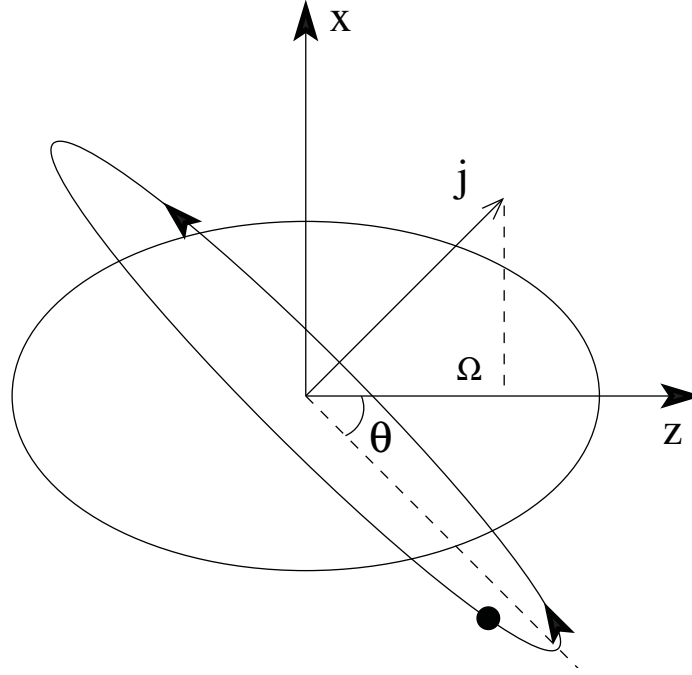


Figure 9: Sketch of a nucleon orbiting a deformed nucleus.  $j$  is the total angular momentum and  $\Omega$  is the projection of the angular momentum where  $z$  is the symmetry axis.

Figure 9 shows a sketch of a nucleon orbiting about such a deformed nucleus. From this diagram, we can see that the energy of an orbital depends significantly on the inclination of that orbit. This manifests itself as a parameter called  $\Omega$ , and is defined as the projection of the angular momentum of the nucleon ( $j$ ) along the symmetry axis. As the angle  $\theta$  in Figure 9 becomes smaller and the nucleon tends to orbit around the “equator” of the nucleus,  $\Omega$  will be very small since the direction of angular momentum is normal to the plane of the orbit. Conversely, as  $\theta$  becomes greater and the nucleon’s orbit begins to cross the poles of the nucleus,  $\Omega$  will be rather large. In the latter scenario, the nucleon spends most of its orbit a substantial distance from the core of the nucleus when compared to the former. Accordingly, such highly-inclined orbits require the nucleon to have significantly more energy than equatorial orbits. Because of this, we can use  $\Omega$  as a measure of the sequential energy ordering of various orbitals within a shell. The energy dependence on  $\Omega$  breaks the  $2j + 1$  degeneracy of the shell model states and will be critically important for later calculations.

When applying the deformation of the nucleus to the shell model, the primary consideration is ensuring that the particle in question is affected by a non-spherical orbital of the form:

$$V(r) = V_0(r) + V_2(r)P_2(\cos \theta) \quad (8)$$

where  $P_2(\cos \theta)$  is the second-order Legendre Polynomial and serves to deform the potential along the symmetry axis. Traditionally, the symmetry axis is assumed to be the  $z$  axis of a Cartesian co-

ordinate system. The actual form of the potential, beyond the inclusion of a deformation parameter, is mostly a matter of preference. Some theoretical calculations employ the Woods-Saxon potential which does yield more accurate results (since the Woods-Saxon potential is a good description of reality as discussed earlier), but here we will use the more basic harmonic oscillator potential to simplify the presentation.

In order to employ this new model in theoretical calculations, we write down the *Hamiltonian* of the system, which is the sum of the system's kinetic and potential energy and therefore represents the total energy of the system at any time ( $H = T + V$ ) [16].

$$H = \frac{\mathbf{p}^2}{2m} + \frac{1}{2}m [\omega_x(\mathbf{x}^2 + \mathbf{y}^2) + \omega_z\mathbf{z}^2] + C\ell \cdot \mathbf{s} + D\ell^2 \quad (9)$$

The first term,  $\frac{\mathbf{p}^2}{2m}$ , satisfies the inclusion of the kinetic energy ( $T$ ) of the nucleon in the Hamiltonian. It is the familiar form of  $T = \frac{1}{2}mv^2$  with the momentum of the nucleon substituted for its velocity ( $p = mv$ ).

The second term is the potential of the nucleon within the harmonic oscillator potential. Each  $\omega_i$  term represents the oscillation frequency in each direction of the coordinate system. For an isotropic, three-dimensional oscillator, this would be of the form  $\frac{1}{2}m\omega r^2$  where the spherical coordinate  $r$  can be converted to a Cartesian coordinate system as  $r^2 = x^2 + y^2 + z^2$ . However, the deformation around the  $z$  axis necessitates the separation of the frequencies since the deformed situation has  $\omega_x = \omega_y \neq \omega_z$ .

The third term is the familiar spin-orbit interaction presented previously, and the fourth term applies corrections to high- $\ell$  nucleons to ensure the magic numbers are properly returned. The expanded coefficients on these terms are  $C = -2\hbar\omega_o\kappa$  and  $D = -\hbar\omega_o\kappa\mu$ . The particular values of  $\kappa$  and  $\mu$  are specific to the shell in question and can be determined by adjusting the parameters to suit experimental data.

### 3.2.1 Deformation Parameters

Though the  $\omega_i$  terms are convenient while working with the harmonic oscillator itself, since we are considering the deformation of the nucleus it is more convenient to write the Hamiltonian using a deformation parameter. There are an unfortunate number of various such parameters employed to describe deformed nuclei. This section will serve as a familiarization of the language used in the context of the deformed shell model before continuing to develop the theory.

1.  $\delta$  is a rather straightforward parameter of deformation and was the original parameter introduced by Nilsson when he first published the model. Although it has a few different definitions, one starting point is to introduce it as a correction to the quadrupole moment ( $Q_0$ ) for a deformed nucleus.  $Q_0$  is essentially a representation of the distribution of charge around the center of the nucleus and, applying the  $\delta$  deformation, has the form [17]:

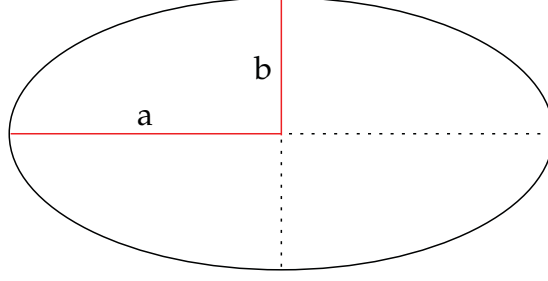


Figure 10: Cross section of a typical ellipsoid. Note the definitions of the semi-major ( $a$ ) and semi-minor ( $b$ ) axes.

$$Q_0 = \frac{4}{3} \left\langle \sum_{k=1}^Z r_k^2 \right\rangle \delta \quad (10)$$

where the sum aggregates the square of the radial position of each proton. With a few basic assumptions about the shape of the nucleus,  $\delta$  can be written as [18]:

$$\delta = \frac{3}{2} \frac{a^2 - b^2}{a^2 + 2b^2} \quad (11)$$

$$\begin{aligned} &\approx \frac{\Delta R}{R_{\text{avg}}} + \frac{1}{6} \left( \frac{\Delta R}{R_{\text{avg}}} \right)^2 + \dots \\ &\approx \frac{\Delta R}{R_{\text{avg}}} \end{aligned} \quad (12)$$

$\Delta R$  is the difference between the semi-major ( $a$ ) and semi-minor ( $b$ ) axes of the ellipsoid ( $\Delta R = a - b$ ). Refer to Figure 10 for an illustration of these dimensions. Here, we define  $R_{\text{avg}}$  as  $R_{\text{avg}} = R_0 A^{1/3}$  with  $R_0 = 1.22$  fm as it is traditionally approximated. We can also use  $\delta$  to consolidate the  $\omega_i$  notation of the deformed shell model. Using  $\delta$ , we obtain [17]:

$$\omega_x^2 = \omega_y^2 = \omega_0^2 \left( 1 + \frac{2}{3} \delta \right) \quad (13a)$$

$$\omega_z^2 = \omega_0^2 \left( 1 - \frac{4}{3} \delta \right) \quad (13b)$$

where  $\omega_0$  is the oscillation frequency of the deformed system. Since the volume of the nucleus is conserved no matter its deformation, the product of its extension along all three axes must be a constant. In other words,  $\omega_x \omega_y \omega_z = \text{constant}$ . We can then write the oscillation frequency for the deformed nucleus as [19]:

$$\omega_0(\delta) = \overline{\omega_0} \left( 1 - \frac{4}{3} \delta^2 - \frac{16}{27} \delta^3 \right)^{-1/6} \quad (14)$$

where  $\overline{\omega_0} = \omega_0(\delta = 0)$ .



2.  $\epsilon$  is the Nilsson quadrupole deformation parameter (and sometimes more explicitly written as  $\epsilon_2$ ).  $\epsilon$  is closely related to  $\delta$  and its existence is due solely to a slight change of notation in the consolidation of the  $\omega_i$  terms [17]:

$$\omega_x = \omega_y = \omega_0 \left( 1 + \frac{1}{3}\epsilon \right) \quad (15a)$$

$$\omega_z = \omega_0 \left( 1 - \frac{2}{3}\epsilon \right) \quad (15b)$$

With the same volume constraint, we find:

$$\omega_0(\epsilon) = \overline{\omega}_0 \left( 1 + \frac{1}{9}\epsilon^2 + O(\epsilon^3) \right) \quad (16)$$

where  $O(\epsilon^3)$  is a Landau Function and signifies that, while the expansion has higher-order terms, they are not significant compared to the explicitly written lower-order terms. The purpose of recasting the deformation in  $\epsilon$  is to remove an approximation from energy calculations that  $\delta$  necessitates but the intricacies of this difference are beyond the scope of this work.  $\epsilon$  can be related to  $\delta$  by [20]:

$$\epsilon = \delta + \frac{1}{6}\delta^2 + \frac{5}{18}\delta^3 + \dots \quad (17)$$

which, to first order, implies  $\epsilon \approx \delta$ .

3.  $\beta$  is the last deformation parameter and is perhaps the most conventionally defined. This parameter describes the first significant deformation level of the multipole expansion of nuclear shape. In a multipole expansion, complex structures are broken down into increasingly complex components called multipoles that are based on spherical structures. For deformations, the sequence of multipoles goes monopole, quadrupole, octopole, hexadecapole, and so on. Although the higher-level deformations do exist in nuclei, they are so small compared to the lowest order deformations that neglecting them significantly simplifies our analysis without greatly affecting the result. The full expression of the radius of the deformed nucleus is [11]:

$$R(\theta, \phi) = R_0 \left[ 1 + \sum_{\lambda=0}^{\infty} \sum_{\mu=-\lambda}^{\mu=\lambda} \alpha_{\lambda\mu} \mathbf{Y}_{\lambda\mu}(\theta, \phi) \right] \quad (18)$$

where  $\theta$  and  $\phi$  are angular spherical coordinates,  $\alpha_k$  are the expansion coefficients, and  $\mathbf{Y}_{\lambda\mu}(\theta, \phi)$  are known as spherical harmonics which apply the deformation. The  $\lambda$  index determines the order of the expansion.  $\lambda = 0$  is the monopole term,  $\lambda = 1$  is the dipole term, and so on. However, the first term that actually deforms the nucleus is the  $\lambda = 2$  dipole term. The monopole term is a simple change in its radius which contradicts our earlier assumption that volume is conserved. Thus, the  $\lambda = 0$  term does not exist. Similarly, the dipole term represents the displacement of the entire nucleus which cannot exist without an external

force. Therefore,  $\lambda = 1$  is also not permitted. As such, we limit ourselves to the  $\lambda = 2$  term with the understanding that, while higher-order deformations may be present in the nucleus, they are insignificant when compared to the quadrupole deformation. Our sum then reduces to:

$$R(\theta, \phi) = R_0 \left[ 1 + \sum_{\mu=-2}^{\mu=2} \alpha_{2\mu} Y_{2\mu}(\theta, \phi) \right] \quad (19)$$

Thus, there are 5 individual  $\alpha_{2\mu}$  components. Due to the nature of the various spherical harmonics,  $\alpha_{11} = \alpha_{2,-1} = 0$  since these terms represent translational motion that we are not considering [7]. Accordingly, we are left with the following three coefficients which can be written using two new parameters [11]:

$$\alpha_{20} = \beta \cos \gamma \quad (20a)$$

$$\alpha_{22} = \alpha_{2,-2} = \frac{1}{\sqrt{2}} \beta \sin \gamma \quad (20b)$$

The particulars of the terms are not important beyond defining the existence of the new deformation parameters  $\beta$  and  $\gamma$ . As mentioned earlier,  $\beta$  represents the quadrupole deformation of the nucleus. The new parameter  $\gamma$  represents the *triaxial* deformation of the nucleus. The interplay between quadrupole deformations and triaxial deformations will play a central role in our argument of the nature of  $^{160}\text{Lu}$ . Figure 11 illustrates a systematic way of classifying deformations in terms of  $\beta$  and  $\gamma$  known as the Lund convention.

Though  $\gamma$  is a fundamentally different kind of deformation than  $\delta$  and  $\epsilon$ ,  $\beta$  can be related to the previous quadrupole deformations by [20]:

$$\beta = \sqrt{\frac{\pi}{5}} \left( \frac{4}{3}\epsilon + \frac{4}{9}\epsilon^2 + \frac{4}{27}\epsilon^3 + O(\epsilon^4) \right) \quad (21)$$

To first order, we can approximate  $\beta \approx 1.05\epsilon \approx 1.05\delta$ .

All three quadrupole deformation parameters are very similar, particularly for the small deformations we are dealing with in this nuclear region. It is important to understand that they are indeed different quantities and are not arbitrarily defined. That being said, we will proceed with the use of  $\beta$  and  $\gamma$  as the deformation parameters of choice in the remainder of this work.

The deformation parameters allow nuclei to be broken into two categories: deformations with  $\beta < 0$ , known as oblate nuclei, and deformations with  $\beta > 0$ , known as prolate nuclei. Figure 12 illustrates these classifications.

As alluded to earlier, the most important result of the deformed shell model is the ability to analyze the change in the energies of different orbitals as the shape (deformation) of the nucleus changes. Figure 13 shows this phenomenon, known as  $\Omega$  splitting, for a representative orbital. Notice that when the deformation is 0, the energies of all  $\Omega$  states are equal and thus the orbital is degenerate. This type of figure is a very simplistic version of more complex figures called Nilsson

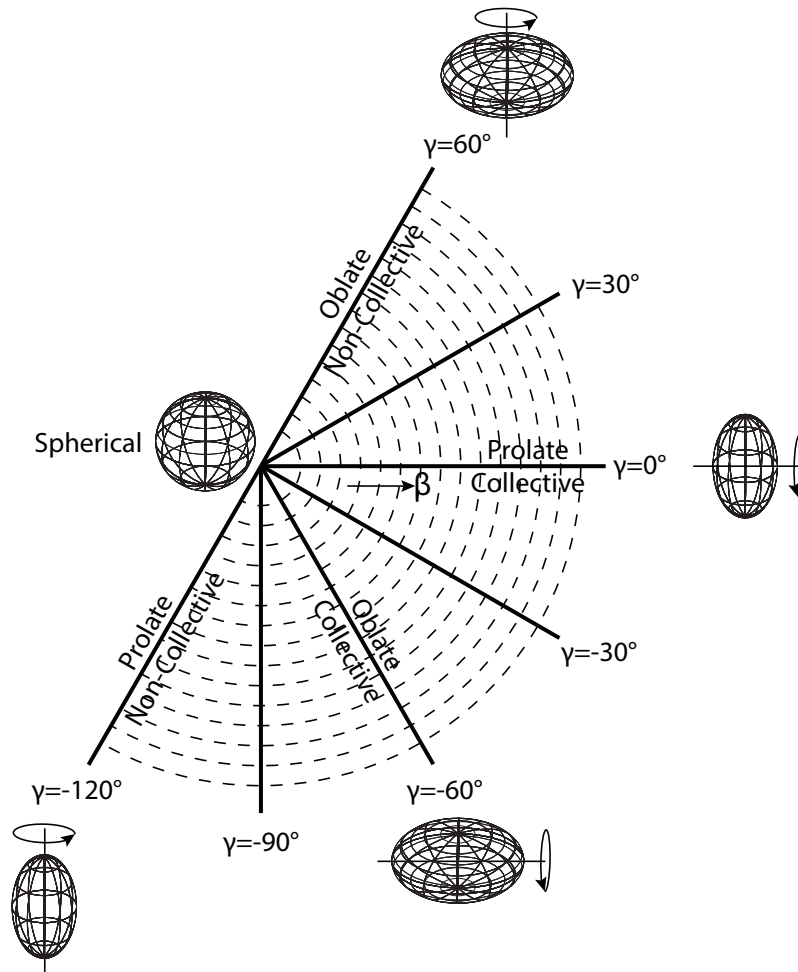


Figure 11: The Lund Convention for nuclear deformations.  $\beta$  gives quadrupole deformations while  $\gamma$  gives triaxial deformations. Adapted from [11].

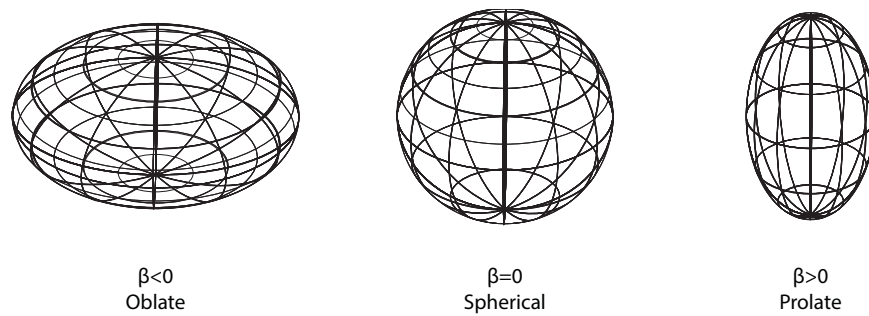


Figure 12: Deformation categories dependent on the sign of  $\beta$ .

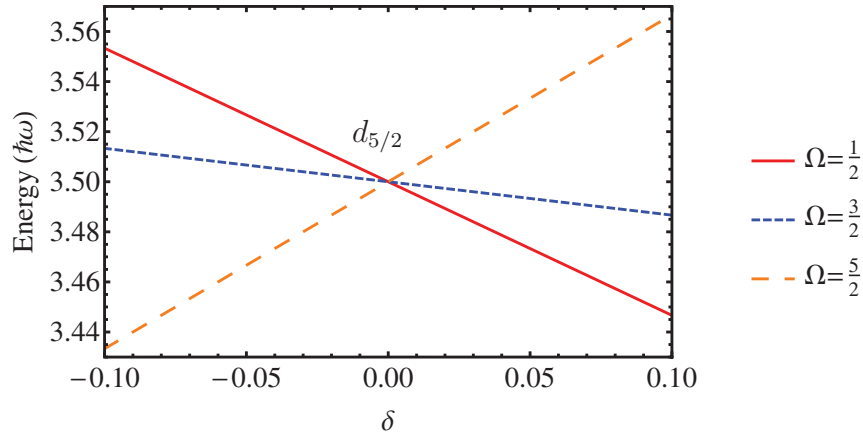


Figure 13: Calculations of  $\Omega$  splitting in the  $1d_{5/2}$  orbital. Note that at  $\delta = 0$  all alignments are degenerate in energy. Energies were calculated using a small- $\delta$  approximation and a perturbation to the spherical harmonic oscillator potential.

diagrams. These diagrams, introduced in Section 7, are tremendously useful in determining the likely configuration of a nucleus at a particular energy and deformation.

One of the key concepts to understand from the Nilsson model and Figure 13 is that once the nucleus exhibits prolate deformation ( $\beta > 0$ ), a nucleon with low  $\Omega$  can orbit that nucleus with lower energy than it could have orbited a spherical potential [7].

### 3.2.2 Nilsson Quantum Numbers

Once the spherical potential has been deformed, we lose the ability to use  $\ell$  and  $j$  to uniquely identify the states. Now, the orientation of the angular momentum determines the energy of the state. This means that various nuclei could have the same total angular momentum but different energies, and thus no longer can be discretely identified by the momenta quantities themselves. The Nilsson orbits are traditionally labeled with a series of five quantum numbers of the form [16]:

$$K^\pi [Nn_z\Lambda]$$

1.  $K$  is the projection of the total angular momentum on the symmetry axis. It is often times conflated with  $\Omega$ , though there is a subtle but nonetheless significant distinction between the projection of the total angular momentum ( $K$ ) and the projection of the *nucleon's* angular momentum ( $\Omega$ ). For a variety of nuclei, particularly those at low rotational frequency, the numerical difference between  $K$  and  $\Omega$  is negligible so both quantities can serve as the first Nilsson quantum number.
2.  $\pi$  is occasionally included in Nilsson labeling and refers to the parity of the orbital. Parity is a representation of the spatial symmetry of the wavefunction. The parity operator maps all spatial coordinates to their opposites (i.e.,  $x \rightarrow -x$ ,  $y \rightarrow -y$ ,  $z \rightarrow -z$ ). If the resulting function is unchanged (as  $x^2$  would be), the system is said to have *even* parity. If the system

returns with the opposite sign, (as  $x^3$  would), it is said to have *odd* parity. When applying the parity operator to the spherical portion of the wave function, the resulting sign goes as  $(-1)^\ell$  which we will take as our definition of the parity of a nuclear orbital.

3.  $N$  is the indexing quantum number and is identical to  $N$  in the spherical shell model.
4.  $n_z$  is the number of nodes that the orbital's wave function has along the  $z$  axis. In other words, it represents how many times the function switches sign. The more nodes the wave function has, the more it is aligned in the  $z$  direction and consequently the lower energy the orbits.
5.  $\Lambda$  is the projection of the orbital angular momentum along the symmetry axis. That is, it is the projection of  $\ell$ . Note that this means  $K = \Lambda + S$  where  $S$  is the projection of the nucleon's intrinsic spin.

An example would serve to better illustrate Nilsson labeling conventions. Consider the  $h_{11/2}$  orbital. Here,  $j = 11/2$  and  $h$  orbitals are associated with  $\ell = 5$ . We will begin by considering the lowest energy orbit which, as we know from Section 3.2, is the most equatorial. The most equatorial orbits have the lowest projected angular momentum, meaning that we will choose  $K = 1/2$ .

However, the orientation of the orbit tells us about the nature of  $n_z$ . At most,  $n_z = N$  due to the indexing nature of  $N$  and its constraints on the size of the wave function. But  $n_z$  is effectively a representation of how extended the wave function is along the  $z$  axis. Since we already decided to consider the most equatorial orbit, the  $K = 1/2$  orbit must have the greatest possible  $n_z$  value, or  $n_z = 5$ . Similarly, successively higher energy  $N = 5$  orbitals will have lower  $n_z$  values.

Finally, having identified  $K$  and  $n_z$ , we come to  $\Lambda$ . Again,  $\Lambda = K \pm S$  which leaves us with either 1 or 0. However, there is one further constraint of  $\Lambda$ . In order to preserve the parity of the orbital (since mixed-parity wave functions are impossible), the quantity  $n_z + \Lambda$  must match the parity of  $N$ . If  $N$  is an odd number (as it is here), the quantity  $n_z + \Lambda$ , too, must be odd. This necessitates  $\Lambda = 0$  and thus for this example we have:

$$K^\pi [N n_z \Lambda] = 1/2^- [550]$$

### 3.3 Pairing Effects

There is a substantial amount of experimental evidence supporting the idea that nucleons pair within the nucleus [7]. Perhaps the biggest hint at this phenomenon is the observation that the ground state of *all* even-even nuclei has spin ( $J$ ) and parity ( $\pi$ )  $J^\pi = 0^+$ . In order for these states with an even number of nucleons to have zero total angular momentum, the angular momenta of the nucleons must cancel out. Further, it is observed that the binding energy *increases* when a nucleon is added to make the nuclei even-even. More of the added mass of the nucleus is converted into binding energy when the even-even state is reached than when an odd- $A$  state is reached. This implies some additional attractive force between even numbers of particles that is less present in odd- $A$  nuclei.

We imagine the pairing force to be the interaction of two nuclei in an orbit with a given  $j$  and  $|\Omega|$ . However, since two particles cannot simultaneously occupy the same orbital, they must be traveling about the nucleus in opposite directions (that is to say, one with  $+\Omega$  and one with  $-\Omega$ ). We say that such nuclei are in *time-reversed* orbits. Thus, the total angular momentum of the pair of nucleons is necessarily zero since each nucleon has the same  $j$  but the opposite direction of motion.

To adopt this view, we must qualify the previous line of reasoning that yielded the conclusion that inner-shell nucleons do not collide. Because they are physically restricted to their respective orbitals but traveling towards each other, the nucleons will inevitably collide and attempt to scatter into other orbitals. The central tenet of this view of pairing is that the colliding nucleons are just as likely to scatter back into their original orbit as they are to scatter into nearby orbitals. If this were not true, we would expect that the energy to create a two-particle excited state in an even-even nucleus would be at least twice as great as the energy required to create a one-particle state in a neighboring odd-A nucleus. As it turns out, the difference in energy is much greater for an even-even nucleus—up to 10 times as great [16]. The underlying cause is the pairing interaction between nucleons which must first be broken (typically requiring  $\approx 2$  MeV of energy) before the individual nucleons can be excited.

Thus, the existence of the pairing interaction requires us to completely alter our understanding of the energy structure of the nucleus. But first, a brief introduction to the vocabulary of statistical mechanics is necessary. In the quantum mechanical realm, states are quantized, meaning that they take on discrete values. Each state has a certain energy associated with it, and consequently a certain probability of being observed. Multiple states can sometimes achieve the same energy though the nature of the states themselves are quite different. This is the concept of degeneracy as was presented in the context of the shell model.

When we imagine a system from the macroscopic level (at the scale of the entire nucleus) rather than the microscopic level (that of an individual nucleon), we see a collection of successively higher energy levels. The term *Fermi surface* (also, Fermi level) is applied to the highest occupied energy level. Excitations of the system can promote nucleons occupying lower states into states above the Fermi surface, but doing so requires energy beyond the “resting” energy the system possesses.

Instead of imagining an energy structure with occupied states up to the Fermi surface and entirely unoccupied states above it, we must envision a series of partially occupied states, though increasingly less so, from the ground state all the way up to the most excited state due to the presence of the pairing interaction. The scattering behavior of the nucleons allows for a general mixing of wave functions of the lower states. These states are no longer strictly filled or unfilled, but rather are in some state of being partially filled. The energies required to more fully populate a partially full state are less than those required to populate empty states, which is the driving force of the alteration of the energy structure. Figure 14 illustrates the nature of these partially-filled levels. With this understanding of the statistical mechanics of the nucleus, we now recognize that the mid- and upper-levels of the nucleus are not populated by particles and “holes” (created by the lack of a particle), but rather by some intermediate state known as a *quasiparticle* (QP) [7].

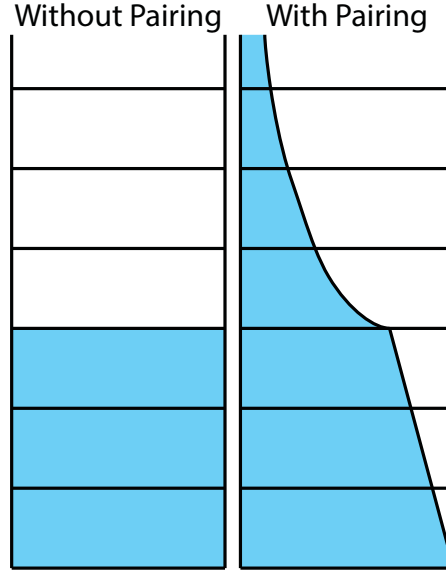


Figure 14: A visual depiction of the filling of energy levels in a system with (right) and without (left) pairing. The amount of shading indicates how filled a given level is. Note on the left graphic, all states are filled below the Fermi level while on the right, all states are partially filled. Adapted from [11].

### 3.4 Cranked Shell Model

There is one final adjustment to our model of the nucleus necessary to specifically address some of the physics related to analyzing rapidly-rotating nuclei. The missing component is the angular momentum of the entire nucleus, as generated by the heavy-ion reaction. We can include it rather directly by building upon the deformed shell model and adding a rotational component to the model. To do so, we must shift our data from the stationary reference frame of the laboratory into the rotating frame of the nucleus. We apply the following coordinate transformation:

$$x' = x \quad (22a)$$

$$y' = y \cos(\omega t) + z \sin(\omega t) \quad (22b)$$

$$z' = -y \sin(\omega t) + z \cos(\omega t) \quad (22c)$$

Which subsequently introduces a slight modification to our deformed shell model Hamiltonian and yields the Hamiltonian for the cranked shell model (CSM) known as the *Routhian*:

$$H' = H - \omega J_x \quad (23)$$

where  $\omega$  is the rotational frequency of the nucleus and  $J_x$  is the angular momentum operator along the  $x$  axis.

Referring to Figure 9, note that the  $x$  axis is perpendicular to the symmetry axis ( $z$  axis). The term “symmetry axis” is not used in the classical sense of an axis on either side of which the object is identical. Rather, the symmetry axis is an axis around which spin is not possible. Consider a



floating metal sphere that is both perfectly round and perfectly polished to a mirror finish without blemishes or imperfections. As the sphere is observed, there is no possible way to determine if it is spinning or not. No matter whether it is stationary or rotating around any coordinate axis, the surface area it presents will always perfectly reflect its surroundings. Under the rules of quantum mechanics, if it is not possible to directly observe an event, it is impossible for that event to occur. As such, any object possessing a symmetry axis cannot exhibit rotation about that axis [18].

Beyond this, if we define both of the mutually perpendicular  $x$  and  $y$  axes, we cannot say for certain about which the nucleus will rotate. However, we have the freedom to select our own coordinate system and therefore can arbitrarily define rotation to occur about the  $x$  axis. Thus, we employ  $J_x$  and not  $J_y$ . Regardless, rotations about  $J_x$  or  $J_y$  are identical. Since we could not distinguish a rotation about  $J_x$  from one about  $J_y$ , our choice truly is at our discretion.

By this point in our increasingly complex picture of the nucleus, we have all but exhausted analytic means of studying our models. The CSM requires numerical solutions, though a description of the approaches necessary to run CSM calculations is far beyond the scope of this work. However, we will discuss the implications of the additional  $\omega J_x$  term that is now exerted on the nucleus.

### 3.4.1 CSM Quantum Numbers

Now that the Routhian is time dependent, we lose the ability to use momenta or projections of momenta of any sort as quantum numbers since the values are constantly changing. As such, we are left with two good quantum numbers in the cranking model:

1. Parity ( $\pi$ ), as before, remains a valid quantum number reflecting the spatial invariance of the Routhian.
2. Signature ( $\alpha$ ) is a quantity that arises from the symmetry of the Routhian about the  $x$  axis. Since we arbitrarily defined the rotation of the system to occur about the  $x$  axis, this symmetry arises naturally. The rotation operator is defined as  $\mathcal{R}_x = e^{-i\pi J_x}$ . The application of this operator yields a rotation of  $2\pi$  which means that systems with even mass numbers ( $A$ ) are unaffected while systems with odd mass numbers reverse sign. Thus, we have:

$$\mathcal{R}_x^2 = (-1)^A \quad (24)$$

When applying operators to wave functions, the phrase “eigenvalue” is often used to describe the result. An eigensystem is a system in which there is an operator (such as the momentum operator) which, when applied to some function (in our case a wave function describing a state), yields that same function multiplied by a constant value. The value that results is the eigenvalue.

The eigenvalue of the rotation operator is the signature quantum number and can be written as:

$$r = e^{-i\pi\alpha} \quad (25)$$



Label	Designation $(\pi, \alpha)_n$
A	$(+, +1/2)_1$
B	$(+, -1/2)_1$
C	$(+, +1/2)_2$
D	$(+, -1/2)_2$
E	$(-, -1/2)_1$
F	$(-, +1/2)_1$

Table 1: Notation for CSM quantum numbers. The  $n$  subscript refers to the sequential energy levels of each set of orbitals.  $n = 1$  is the lowest orbital,  $n = 2$  the next highest, and so on.

For the integer spin of a given state  $J$ , we have

$$r = (-1)^J \quad (26)$$

which produces a variance in the signature for even and odd spins as follows:

$$\begin{array}{ll}
 r = +1 \ (\alpha = 0) & \text{for } J = 0, 2, 4, \dots \\
 r = -1 \ (\alpha = -1) & \text{for } J = 1, 3, 5, \dots
 \end{array}
 \left. \vphantom{\begin{array}{l} r = +1 \\ r = -1 \end{array}} \right\} \text{For even-}A \text{ nuclei}$$

$$\begin{array}{ll}
 r = -i \ (\alpha = +\frac{1}{2}) & \text{for } J = \frac{1}{2}, \frac{5}{2}, \frac{9}{2}, \dots \\
 r = +i \ (\alpha = -\frac{1}{2}) & \text{for } J = \frac{3}{2}, \frac{7}{2}, \frac{11}{2}, \dots
 \end{array}
 \left. \vphantom{\begin{array}{l} r = -i \\ r = +i \end{array}} \right\} \text{For odd-}A \text{ nuclei}$$

Though  $r$  is technically what the word “signature” refers to, it is far more common to employ  $\alpha$  and its associated values to describe signature, so that convention will be continued in this work.

We will frequently encounter a method of consolidating these quantum numbers into single-letter abbreviations for various unpaired particles [21]. This notation is summarized in Table 1.

### 3.4.2 Coriolis Effects

The Coriolis effect or the Coriolis force is most traditionally discussed in the context of deflections of the trajectory of projectiles on Earth. If we consider a rocket launched from the equator on a trajectory due north, it will not only have a northward velocity due to its intended trajectory, but it will also have a component of eastward velocity that the easterly rotation of the Earth gives it upon launch.

However, the surface of the Earth does not rotate at a uniform velocity at every latitude. Since the entirety of the Earth completes one rotation per day and a point on the equator is physically farther from the rotational axis than a point in Alaska, the former point must have a greater velocity than the latter in order to complete a larger rotation in the same amount of time.

Though this easterly component of velocity is negligible over short distances (since it is irrelevant as long as the rocket is interacting with portions of the Earth with equal angular velocities as the launch site), as the rocket progresses North, it will begin to travel in regions where that angular

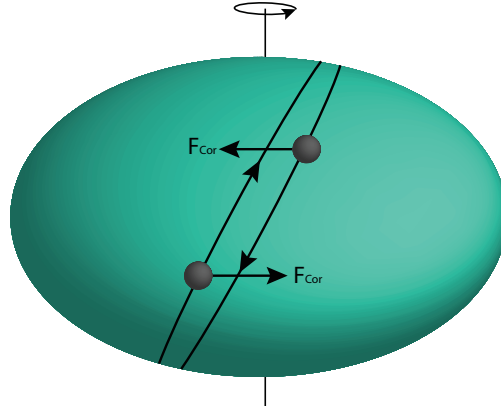


Figure 15: Diagram of the forces exerted on two nucleons in time-reversed orbits.

velocity is considerably less. At the equator, where the angular velocity of the Earth equals the angular velocity of the rocket, the rocket could travel North unaffected. However, once it reaches substantially higher latitudes, its angular velocity becomes much greater than that of the Earth beneath it. Accordingly the rocket appears to begin to travel to the East and its overall trajectory appears to be deflected clockwise (to the right) of its intended path. See Figure 15 for an illustration of this effect.

The force that generates this deflection is called the Coriolis force and is present whenever moving objects are analyzed within a rotating reference frame. The magnitude of the force is given by:

$$F_C = -2m\Omega_v \times \mathbf{v} \quad (27)$$

where  $m$  is the mass of the object,  $\mathbf{v}$  is its velocity, and  $\Omega_v$  is the overall angular velocity vector of the reference frame.  $\times$  represents the vector cross product between  $\Omega_v$  and  $\mathbf{v}$  and returns a mutually perpendicular vector (since the resulting Coriolis force indeed acts perpendicularly to these two vectors).

Since this force does apply to any moving object in any rotating reference frame, it surely applies to nucleons orbiting a spinning nucleus. In fact, the  $\omega J_x$  term of the Routhian is the origin of this effect in the nucleus. Upper limit calculations on the strength of the Coriolis force in the nucleus reveal that it can be on the order of the spacings between energy levels of the uncranked nucleus. Clearly, we cannot ignore its effects.

The Coriolis force acts to alter the nucleon's trajectory about the nucleus, which can more correctly be thought of as a "tipping" of the orbit's angular momentum. The net result is that the Coriolis force changes the nucleon's  $\Omega$ . These changes to the projections of the orbitals cause combinations of these states to occur, a phenomenon known as admixing. Coriolis mixing's effects on nucleon orbits will be discussed later.

Perhaps one of the most consequential outcomes of the Coriolis force is the Coriolis anti-pairing effect (CAP). As mentioned in section 3.3, there exists an energetically-favorable pairing interaction between nucleons in time-reversed orbits. Since these orbits have opposite values of  $\Omega$ , the

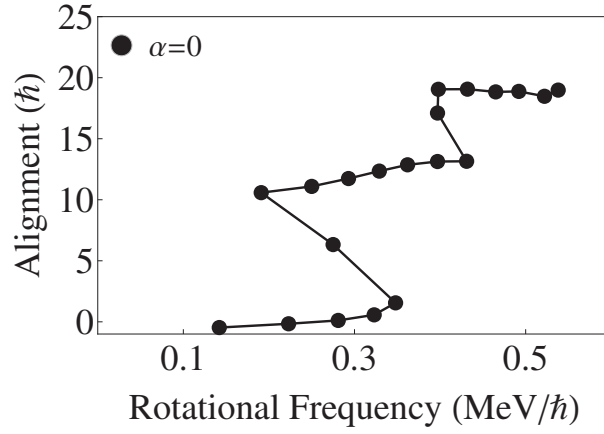


Figure 16: Aligned angular momentum (or alignment) versus rotational frequency for  $^{162}\text{Hf}$ .

Coriolis force will yield an opposite force on each particle. The magnitude of the force is dependent both on the  $j$  of the orbital and the overall rotational velocity of the nucleus ( $\omega$ ), but in general the CAP acts antagonistically to the pairing effect.

In general, we can predict energy levels of the excited bands by approximating the nucleus as a rigid rotor, meaning that it spins as if it were a solid object. For a rigid rotor, the energy of a nucleus with a given spin (rotational velocity)  $J$  is:

$$E_J = \frac{\hbar^2}{2\mathfrak{I}} J(J+1) \quad (28)$$

Where  $\mathfrak{I}$  is the nucleus' moment of inertia, a representation of how its mass is distributed and how difficult it is to spin. Thus, as the nucleus is spun increasingly rapidly, we expect the energy of its levels to increase as  $J(J+1)$ .

However, at sufficiently high spins, the Coriolis force can become strong enough to overwhelm the pairing interaction and decouple, or break apart, the nucleon pairs. In essence, the nucleus enters a regime where it is more energetically favorable to forgo the pairing interaction and create a two-quasiparticle state than it is to continue to excite the coupled nucleons. As a result, the nucleus can gain angular momentum while slowing its rotation. The angular momentum gained by breaking apart the pairing of two particles allows for this gain in overall spin while slowing rotation. Figure 16 shows this effect near a rotational frequency of 0.3 MeV in  $^{162}\text{Hf}$ , plotting the aligned angular momentum from unpaired quasiparticles versus rotational frequency. The dramatic increase in angular momentum accompanied by a decrease in rotational frequency is known as *backbending* or a *band crossing* in the nucleus. As this happens, the nucleus can gain  $(2j-1)\hbar$  of angular momentum at the energy cost of twice the mass difference stemming from the loss of paired binding energy [22]. Thus, we typically see such band crossings for the highest  $j$  orbitals in the nucleus.

### 3.4.3 Band Crossings

We are able to employ CSM calculations to determine the energies of quasiparticles in various orbitals as the rotational energy ( $\hbar\omega$ ) of the nucleus increases. Using such plots, it is possible to predict where these band crossings will occur. We will use Figure 17, showing the Routhians for neutron quasiparticles in  $^{162}\text{Hf}$ , to further elucidate the nature of band crossings. In doing so, we can compare these theoretical predictions with the observed data presented in Figure 16.

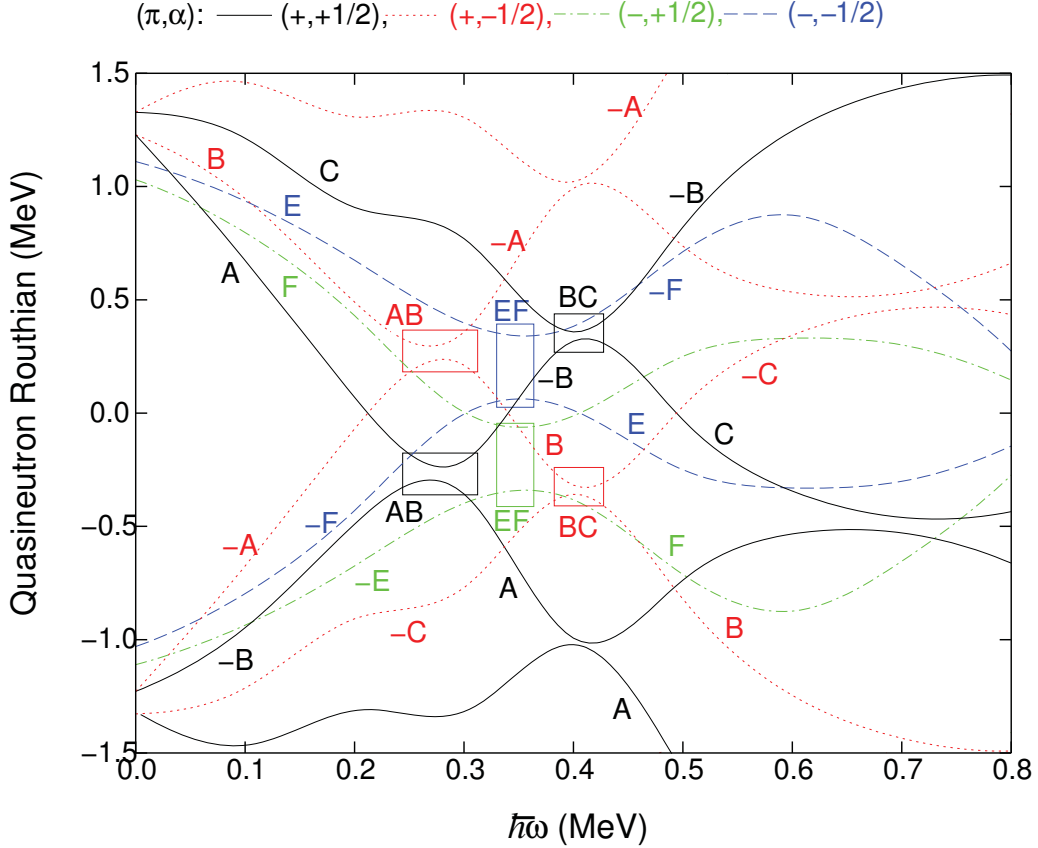


Figure 17: Quasineutron energies vs. rotational energy of  $^{162}\text{Hf}$ . Accordingly to conventional labeling practice, several trajectories have been labelled as well as the locations of three prominent crossings. Deformation parameters employed in our calculations were  $\beta_2 = 0.16$ ,  $\beta_4 = -0.01$ , and  $\gamma = 0$  [23].

Only a select few Routhians are displayed in Figure 17 to aid in the understanding of the significance of each line. The terms “Routhian,” “trajectory,” and “orbital” can all be used interchangeably to refer to these lines. As presented earlier, each quantum number configuration is assigned a letter label as indicated on the figure (see Table 1 for a summary of this notation). Further, the  $y = 0$  line corresponds roughly to the Fermi surface within the nucleus. Of course, the Fermi surface is not so discretely defined, but it serves a useful purpose in distinguishing energy levels that are predominantly full from those that are predominantly empty. Note that the positive-energy orbitals all have a corresponding negative-energy orbital with the same parity but the opposite sig-

nature known as *conjugate* orbitals. These are labeled with a “−” prefix. The  $-A$  orbital is the mirror image of the  $A$  orbital, but with the opposite signature.

One of the fundamental principles behind using such diagrams is the premise that each orbital is either filled with a quasiparticle (QP) or a quasi-“hole”—the absence of a quasiparticle. Moreover, each pair of orbitals ( $A$  and  $-A$ ,  $B$  and  $-B$ , and so on) may only hold one QP. Thus, if there is a QP in  $A$ , by definition there must be a hole in  $-A$ .  $^{162}\text{Hf}$  is a convenient starting point for simplicity as it has no unpaired particles in its ground state.

Returning to our understanding of the Fermi level as the designation of where the levels are 50% filled, any unpaired particles must by definition lie above the Fermi level. From this, it follows that all of the positive-energy orbitals we see in the diagram are empty except for ones that hold unpaired neutrons. Consequently, all of the negative-energy orbitals are full for an even-even nucleus like  $^{162}\text{Hf}$ .

It is critically important to realize that the trajectories of each orbital do not map to the continuous lines on the diagrams, but rather the slopes of the lines. For instance, examine the beginning of the  $A$  trajectory. The black solid line represents the  $A$  orbital up until  $\approx 0.28$  MeV at which point there is an inflection. The  $A$  orbital continues on the lower black line which formerly was the  $-B$  orbital. Then, this new line continues to represent the  $A$  particle until the next inflection point, where  $A$  jumps to the next discontinuous  $(+, +1/2)$  line. These inflection points are doubled as each conjugate pair of orbitals will interact with its respective conjugate pair.

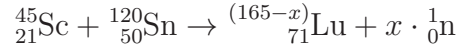
Consider the situation of  $^{162}\text{Hf}$ , an even-even nucleus with no unpaired particles. As we have demonstrated, this means that all of the negative-energy trajectories are populated, and all of the positive-energy trajectories are populated with holes. Following the  $-A$  trajectory up as rotational energy (or frequency) increases, we come to the inflection point between  $-A$  and  $B$ . The QP will naturally attempt to place itself in the lowest energy state available to it. At the inflection, the QP has two choices. It could transition into the downsloping  $B$  orbital, or it could remain in the upsloping  $-A$  orbital. The lowest energy option is clearly to make the  $B$  transition such that now a QP exists in the  $B$  trajectory and a quasihole exists in the  $-A$  trajectory. This is called the  $AB$  band crossing.

Now consider an odd- $A$  nucleus that has a single unpaired neutron. We will assume this neutron is located in the  $A$  trajectory. Again, by definition, this implies that  $-A$  has a hole. Now, when the particle in the upsloping  $-B$  trajectory approaches the  $AB$  interaction at  $\approx 0.28$  MeV, it encounters a quasiparticle in the upsloping  $-B$  trajectory. The particle has nowhere to go in the new orbital and is forced to continue along the upsloping  $-B$  trajectory. In this situation, we say that the  $AB$  crossing is *blocked*. However, as we continue to follow the  $-B$  trajectory to higher frequencies, there is another inflection with the  $C$  orbital that is not occupied. Therefore, the  $-B$  quasiparticle will transition to the downsloping  $C$  orbital, which is called the  $BC$  crossing. Note that the  $-C$  and  $B$  trajectories undergo the same effect.

We will continue to make use of these diagrams and the CSM to interpret our experimentally observed band crossings.

## 4 Experiment

To begin this analysis, the  $^{160}\text{Lu}$  isotope of interest must be generated. The primary method for producing isotopes for nuclear structure research is a heavy-ion reaction. For this experiment, high-spin states of  $^{160}\text{Lu}$  were populated using the reaction:



The general overview of this a reaction is given in Figure 18, with the individual steps outlined below. In this reaction, a beam consisting of heavy-ions ( $^{45}\text{Sc}$ ) is accelerated and directed towards a target of nearly pure isotopic material ( $^{120}\text{Sn}$ ) (Stage 1). Due to the immense energy of the particle beam in the accelerator, the ions have enough energy to overcome the repulsive Coulomb force between themselves and the target. When the ions collide with the target isotope, an intermediate state is formed which is a hybrid of both the incident ion and the target isotope (Stage 2). The resulting nucleus will then give off a number of nucleons (in this case, all neutrons) to quickly reduce its excitation energy (Stage 3).

The beam will very rarely strike the target nuclei at their center of mass and thus will create large amounts of angular momentum in the compound nuclear system. This process is much the same as giving a cue ball english in billiards. If the cue strikes the ball at its center, the ball will travel directly away from the cue. However, if the cue strikes the ball anywhere else, the ball will begin to rotate with non-zero angular momentum as it moves away from the cue. After the nucleus is placed in this rotating excited state, it will seek a lower energy state by losing energy through the emission of gamma rays (Stage 4). Finally, the nucleus reaches its ground state in which it has no excitation energy (Stage 5). The entire process is very quick; it takes place over roughly 1 nanosecond.

The reaction diagram indicates that the heavy-ion reaction will produce various nuclei as products depending on how many nucleons are released after a given collision. This is entirely probabilistic, and eventually the sum-total of data seen by Gammasphere must be partitioned by nucleus before it can be meaningfully analyzed. The fact that such a variety of information is produced by the experiment allows many collaborators to analyze different phenomena in different nuclei without redundancy. Indeed, the data from this experiment will be distributed among a variety of research teams, with this project specifically looking at the resulting  $^{160}\text{Lu}$  data. Although separating the  $^{160}\text{Lu}$  data from the rest may seem daunting, work has already been done in identifying some of the gamma energies associated with  $^{160}\text{Lu}$ .

The data was collected over 3 days in March of 2014. The  $^{45}\text{Sc}$  beam ran at an energy of 215 MeV. The  $^{120}\text{Sn}$  target consisted of a back-to-back stack of two individual targets, one  $\approx 500 \mu\text{g}/\text{cm}^2$  and the other  $\approx 600 \mu\text{g}/\text{cm}^2$ .

In order to capture as many gamma rays as possible while using small detectors, this project utilized Argonne National Laboratory's (ANL) Gammasphere—an array of over 100 small, Compton suppressed HPGe detectors arranged into a sphere. Such a large number of detectors is crucially important for this work, as the decay bands that are being studied are very rarely produced by the heavy-ion reaction.

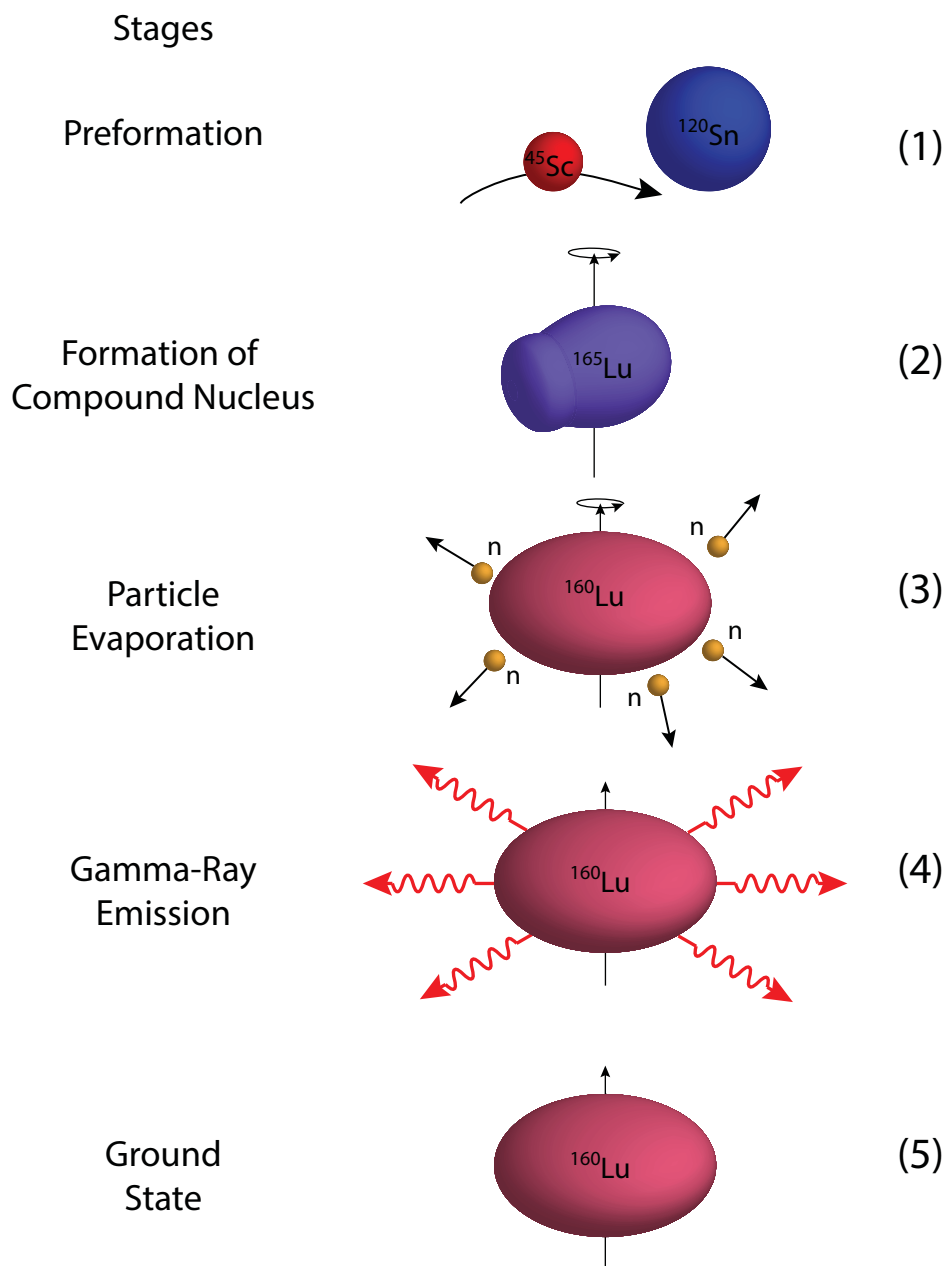


Figure 18: Steps of the Formation of a Compound Nucleus in a Heavy-ion Reaction. Adapted from [11].

## 5 Data Processing

Though a thorough analysis of the data is the crux of this experiment, preliminary data processing requires a significant amount of work. A number of data-correction steps must be taken before the analysis can begin.

### 5.1 Detector Calibration

The first step was to calibrate the detectors. The detectors in Gammasphere register the presence of a gamma ray as a burst of voltage read by an analog-to-digital converter (ADC). Essentially, this is the hardware that allows the data to be digitized by translating the voltage produced in the semiconductor into a digital signal. The key for analysis is to convert the ADC voltage (referred to as a *channel number*) to a meaningful energy corresponding to the energy of the original gamma ray. To perform the calibration, a set of data was taken with  $^{152}\text{Eu}$  and  $^{182}\text{Ta}$  sources. These particular isotopes have very well-measured energies over a large range (100 keV - 1400 keV). By comparing the channel number given by the ADC to the expected energies of various  $^{152}\text{Eu}$  gamma emissions, an equation translating the channel numbers into energies can be determined. Figure 19 shows the peaks of a  $^{152}\text{Eu}$  with the correct energies overlaid.

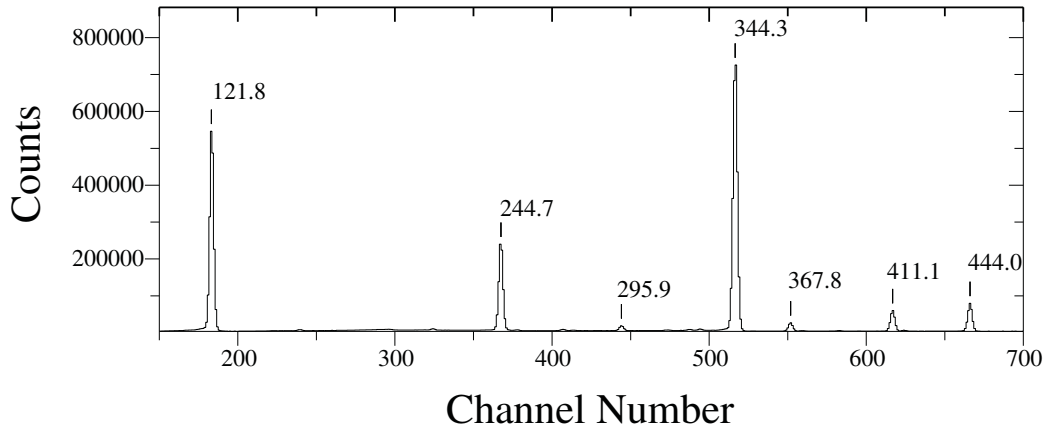


Figure 19: Spectrum of a  $^{152}\text{Eu}$  source for detector calibration. Note the difference between the energies (given in units of keV) labeled on the peaks and the corresponding position of the peak on the  $x$  axis. The difference is the conversion of a channel number to an energy, and can be determined with Equation 29.

After sorting the data from the calibration runs, the calibration spectra were loaded into a spectrum analysis program called `gf3` [24]. The program displays the counts versus the channel number of the gamma rays, as shown in Figure 19. Using the peak-marking feature to identify the channel of the known peaks of the two isotopes in question, we could then match the channels to the known energy associated with particular peaks. The result of this, combining both  $^{152}\text{Eu}$  and  $^{182}\text{Ta}$  data, produces a nearly linear equation that allows for the conversion of channel number into an energy. Using a least squares fitting routine, we determined this equation to be:



$$E = -4.89 \times 10^{-7}x^2 + 6.68 \times 10^{-1}x - 6.44 \times 10^{-1} \quad (29)$$

where  $E$  is the energy of the gamma ray and  $x$  is the channel number read by Gammasphere.

## 5.2 Efficiency Correction

The second correction was to account for the fact that the Gammasphere detectors cannot detect all energies of gamma rays with the same efficiency. Gamma rays with higher energies typically Compton scatter multiple times before they are fully absorbed. The greater the number of scattering events that occur, the greater the likelihood of that gamma being scattered out of the detector. Thus, the detectors typically have a greater efficiency for lower-energy gamma rays. In order to ensure that the observed intensities are representative of the actual intensity, it is necessary to account for this efficiency effect. Just like the calibration, the correction of gamma-ray efficiency can also be done through an analysis of well-studied sources. Here, we again used  $^{152}\text{Eu}$  and  $^{182}\text{Ta}$ . The intensities seen by Gammasphere can be compared to the known intensities and taken as a ratio to determine the relative efficiency,  $\frac{I_{\text{observed}}}{I_{\text{known}}}$ .

Figure 20 shows a plot of the relative efficiencies of a number of  $^{152}\text{Eu}$  and  $^{182}\text{Ta}$  peaks. Two second-order fits of these relative efficiencies were taken over all energies, and then combined to produce the solid line that runs through the points. The equation for this line can be used to interpolate the efficiencies at all energies seen by the detector, and to correct under- or over-represented intensities accordingly.

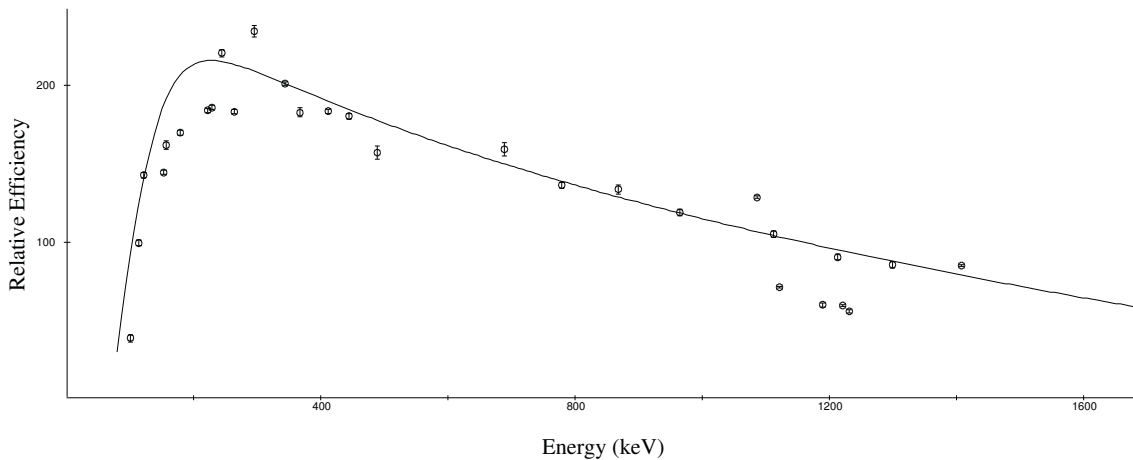


Figure 20: Relative efficiency plot and fit for  $^{152}\text{Eu}$  and  $^{182}\text{Ta}$  sources.

At this point, we are ready to combine all the individual runs of the experiment into a collective file to ease further analysis. The code that performs this task is called BLUE, so the resulting file is referred to as a BLUE database [25]. As the code parses the input files, it sorts all the individual events that the gamma ray detectors observed into *coincidence windows*. That is, it creates a grouping of all the gamma rays that were seen simultaneously by 3 detectors, 4 detectors, and so

on, up to 15 detectors. For the purposes of this work, “simultaneously” means the events occur within the same 80 ns coincidence window.

### 5.3 Doppler Correction

With the created BLUE database, we can now account for the third correction—the Doppler effect. Due to the extremely thinness of the target, the heavy-ion reaction forces nuclei to leave the target when they are struck. Consequently, the compound nucleus of the reaction is moving while it is emitting gamma rays. Since Gammasphere’s detectors are located in rings around the reaction chamber, rings of detectors which are not perpendicular to the beam direction will experience Doppler shifted energies.

Although, as a whole, the impact of broadening the gamma-ray peaks due to the Doppler effect was minimized by using a large number of small area detectors, the position of the peaks will still be affected since the detectors are mounted at different angles with respect to the target. Thus, the detectors will still observe a Doppler shift that will have a significant impact on the data if it is not corrected. To apply the correction, the orientation of each detector with respect to the source must be considered. Gammasphere’s rings are mounted at fixed angles from the target. Since it is known that the ring placed at  $90^\circ$  will not have any Doppler shift, the shifts in gamma energies seen in the spectra of other rings can be compared to this  $90^\circ$  reference and consequently can be shifted accordingly to the correct energy.

Figure 21 shows the effect of the Doppler shift on a number of different rings. The  $90^\circ$  ring is shown in the middle, with forward angles on the top of the figure and backward angles on the bottom. Here, “forward” refers to detectors that are in the direction of the incident beam nucleus on the far side of the target and “backward” detectors are those on the side of the target near the source of the incoming beam nucleus. Reference lines are drawn through a few peaks in the  $90^\circ$  plot. Note that as the angle increases, the difference in the channel number of the gamma ray increases. That is to say, detectors in rings behind the  $90^\circ$  ring record lower energies, while detectors in rings in front of the  $90^\circ$  ring record higher energies. This shift is analogous to the more familiar sonic Doppler shift of a passing train. If one stands in front of a train as it approaches, the sound of the train’s whistle will have a higher tone (frequency) than it actually emits, just as the energies seen by detectors in front of the passing nucleus see higher energy gamma rays than what are actually emitted.

The magnitude of the Doppler shift depends on the velocity of the nucleus, expressed as  $\beta = v/c$  where  $v$  is the velocity of the nucleus and  $c$  is the speed of light. By making a measurement of  $\beta$ , we can determine how much correction needs to be applied to the various angled rings of gamma ray detectors. The energy of the gamma ray seen by a detector at some angle  $\theta$  from the reaction plane is given by

$$E_\gamma = E_0[1 + \beta \cos(\theta)] \quad (30)$$

where  $E_\gamma$  is the Doppler shifted energy,  $E_0$  is the correct energy, and  $\theta$  is the angle of the detector ring.

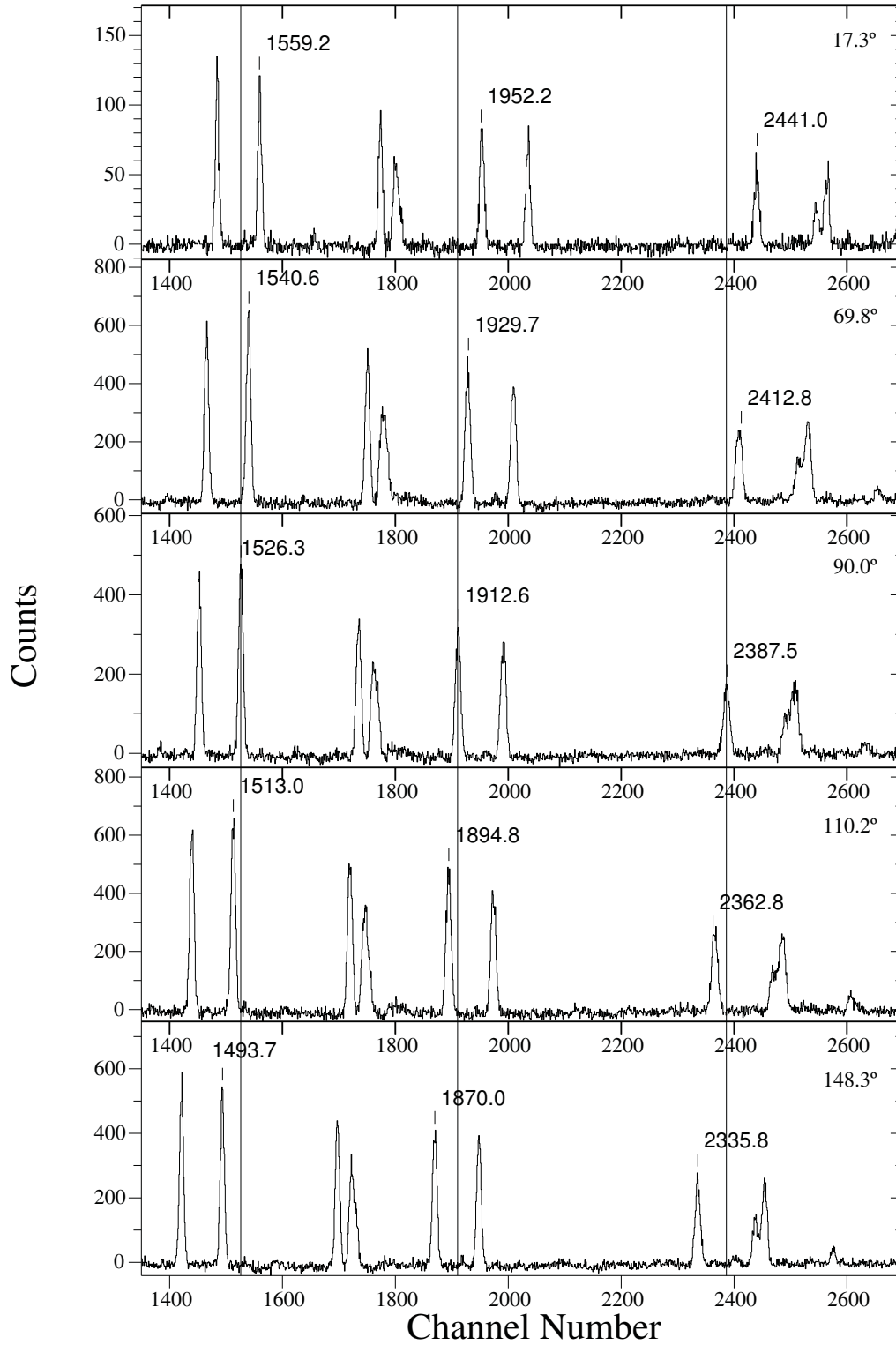


Figure 21: Doppler Shifted Channel Numbers for  $^{160}\text{Yb}$  over a range of detector angles. From top to bottom, 17.3°, 69.8°, 90.0°, 110.2°, and 148.3°. Note that the middle plot of the 90° detector represents the “true” channel numbers.

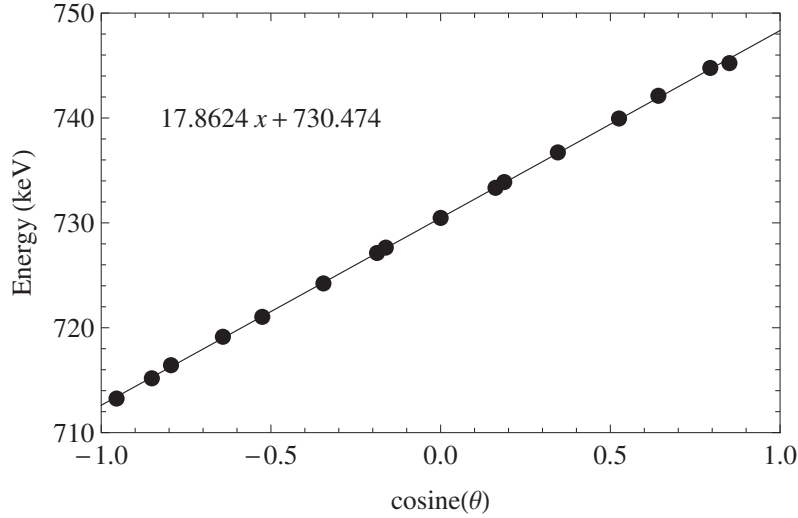


Figure 22: Graph of the progressively Doppler-shifted channel numbers of a gamma ray over all detector rings. Note that the slope is equal to 17.86 with  $E_0=730.474$ . This implies that, for this measurement,  $\beta = 0.0244$  as discussed in the text. The final value of  $\beta$  used in the rest of the work was obtained by averaging many such measurements.

Thus, making a plot of the Doppler shifted energy versus the cosine of the detector angle will produce a line with a slope of  $E_0\beta$  and intercept  $E_0$ . This graph is shown for a gamma ray with channel number equal to 730.4 in Figure 22. We created numerous such graphs for 13 gamma rays across all detector array angles and averaged  $\beta = 0.0255$ . That is to say, on average, the nuclei were traveling at 2.55% of the speed of light. Now that  $\beta$  is known, the peaks can be shifted to their correct values on an event-by-event basis.

Finally, after preparing the data, we must parse the BLUE database into a data cube. The cube is merely a data construct that allows us to identify gamma rays that occur in coincidence with other gamma rays. As will be discussed in the following section, this technique is central to identifying the decay scheme of the nucleus.

## 6 Level Scheme

### 6.1 Level Scheme Theory

If a ball is placed on top of a hill, it is naturally in an unstable state. Although it may initially be at rest, it will eventually roll down the hill—though it is impossible to say exactly which path down the hill it will take. All that is known is that it will start at the top of the hill and end at the bottom. This physical analogy translates to the nuclear realm, as an excited nucleus will want to lose energy and seek a lower energy state, though it is not possible to say with certainty how it will do so. In this experiment, the nuclei involved will decay by emission of gamma rays, and it is generally possible to trace the decay “path” the nucleus takes by observing these emitted gamma rays. Much of the theory of this project is built upon constructing and interpreting what is called a *level scheme* as the result of the data collection, so it is necessary to gain a preliminary understanding of how a level scheme represents the different decay paths the nucleus can take.

In total,  $^{160}\text{Lu}$  has 160 nucleons—71 protons and 89 neutrons. Whenever possible, nucleons like to form pairs. As  $^{160}\text{Lu}$  has an odd number of both protons and neutrons, it is impossible for every proton and every neutron to be in a matching pair. As such, every  $^{160}\text{Lu}$  nucleus will have at least one of each of these particles unpaired, but which nucleons are left unpaired varies. Just as an atom has many different electrons that exist in different orbits and energy levels, so too does the nucleus have protons and neutrons that exist in different energy states. As we have seen, nuclear physicists borrow nomenclature from chemists to describe these protons and neutrons, and so they are labeled based on their “orbital” (s, p, d, and so on) and their spin (always an integer multiple of  $1/2$ ) [7].

The different possible unpaired nucleons lead to different “flavors” of  $^{160}\text{Lu}$  that all have a unique decay sequence associated with having these particular nucleons unpaired. Leaving different nucleons unpaired affects the behavior of the nucleus at higher energies, and consequently the path the nucleus will take down the metaphorical hill to reach a lower energy state. Since different configurations of the nucleus result in different decay paths, it is possible to identify which nucleons are unpaired based on the patterns of energy loss the nucleus displays. These decay paths are revealed in the energies of the gamma rays that are emitted. The resulting information is then compiled in a level scheme, which identifies which gamma emissions are associated with transitions between higher energy states and lower energy states.

Figure 23 shows a small portion of the generally well-established level scheme of a different isotope,  $^{161}\text{Lu}$  [3]. Each horizontal line represents a certain energy level the nucleus can exist at and is labeled to the side with the amount of spin associated with that state ( $39/2 \hbar$ ,  $7/2 \hbar$ , etc.). In between horizontal lines are vertical lines that represent the decay of the higher spin state to the lower spin state through the emission of a gamma ray. The emitted gamma ray has an energy in keV equal to the number the vertical line passes through. Finally, some decay sequences transition into other branches, many of which ultimately feed into the *ground state*, or lowest energy state of the nucleus. These linking transitions (called such because they are transitions that link decay sequences) are indicated by diagonal lines. As a general idea of how different unpaired nucleons affect the decay sequence, Band 1 in Figure 23 is due to the unpairing of the  $h_{11/2}$  proton, while

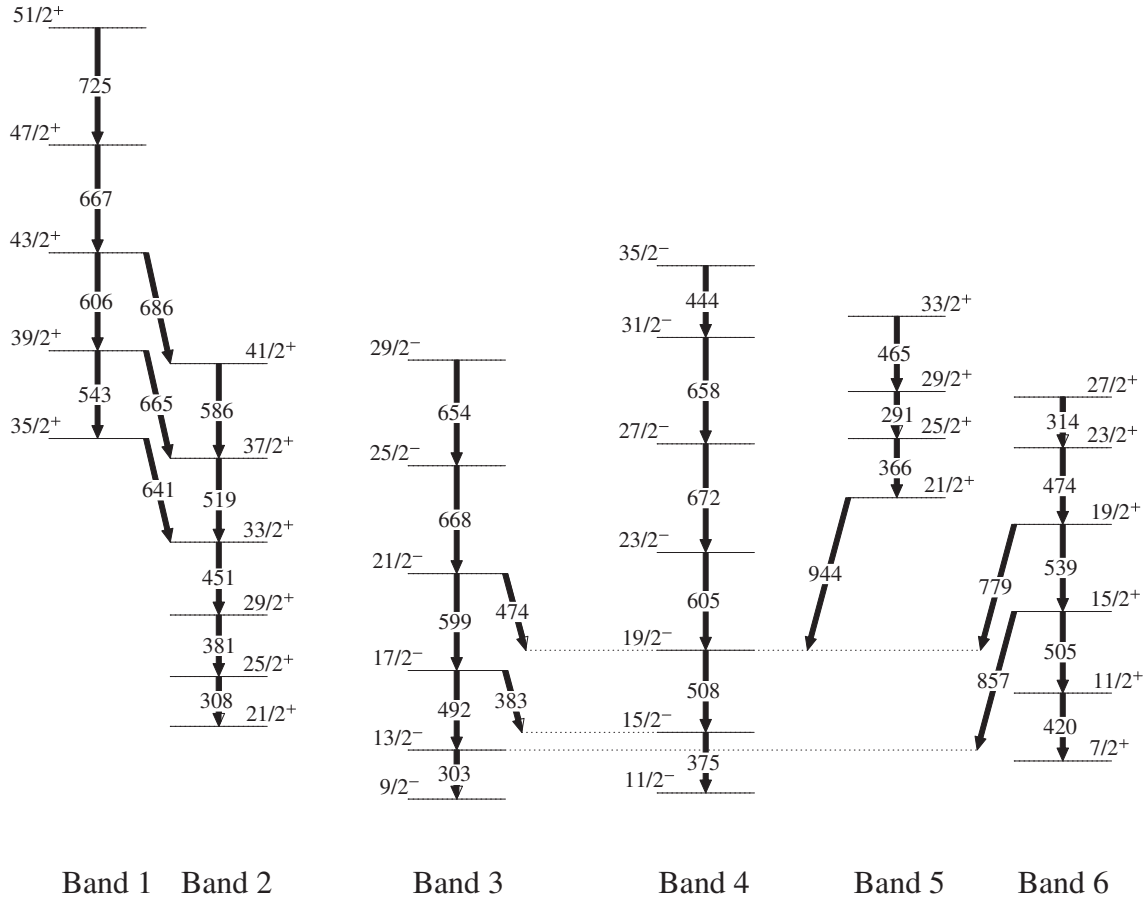


Figure 23: Excerpt of the level scheme for  $^{161}\text{Lu}$ . The different bands are due to different configurations of the nucleus resulting from differing unpaired nucleons [26].

Band 5 results from the unpairing of the  $i_{13/2}$  proton. By detecting the order and grouping of the gamma rays, an overall picture of how different configurations of  $^{161}\text{Lu}$  decay from higher energy levels can be obtained.

The process of creating such a level scheme has been greatly simplified in recent years. In particular, the RADWARE suite of applications developed by David Radford of Oak Ridge National Laboratory has become an essential toolbox for physicists studying nuclear structures [24]. RADWARE's applications have a wide range of capabilities, but this project will specifically use the suite to analyze the coincidence cube, construct the level scheme, and plot parameters of the nucleus, among other tasks.

The steps involved in using the data cube to build a level scheme are shown in Figure 24. Panel A shows the raw spectrum of all gamma rays seen by the detectors. The plot shows the counts the detectors see as a function of the energy of those gamma rays, with higher spikes indicating stronger gamma rays. The first task is to take a *gate* on a particular energy of gamma ray. The word *gate* is used because the process of looking at a single gamma ray's coincidence window narrows the data set, much as passing it through a gate of a given width would do. In the case of Figure 24, the first gate was taken on the 265-keV gamma ray. Panel B shows the result of

this gate. Note that many of the gamma rays that were present in A disappear after taking the gate. This is because gating on 265 keV will only display gamma rays that were detected in the same coincidence window as the 265-keV gamma ray. The gamma rays that disappeared (for instance, the unlabeled 227-keV gamma ray in panel A must have been part of a different decay sequence.

However, this process is not limited to looking at the coincidence windows of a single gamma ray. It is possible to gate on more than one gamma ray energy at once in order to obtain greater clarity and detect even weaker patterns. However, the cost of this clarity is fewer overall statistics as seen in the decreasing intensity of the peaks. Panel C is the result of gating simultaneously on both the 265-keV gamma ray and the 756-keV gamma ray. Thus, C shows the gamma rays that were in the same coincidence windows of both gamma-ray energies. The more gates that are added together, the higher the likelihood of the remaining gammas being part of the same decay sequence is. In fact, after numerous gates it is possible to directly read the decay sequences of stronger bands from the spectrum. The sequence on the right of Figure 24 shows the resulting portion of the level scheme the information in these spectra provides.

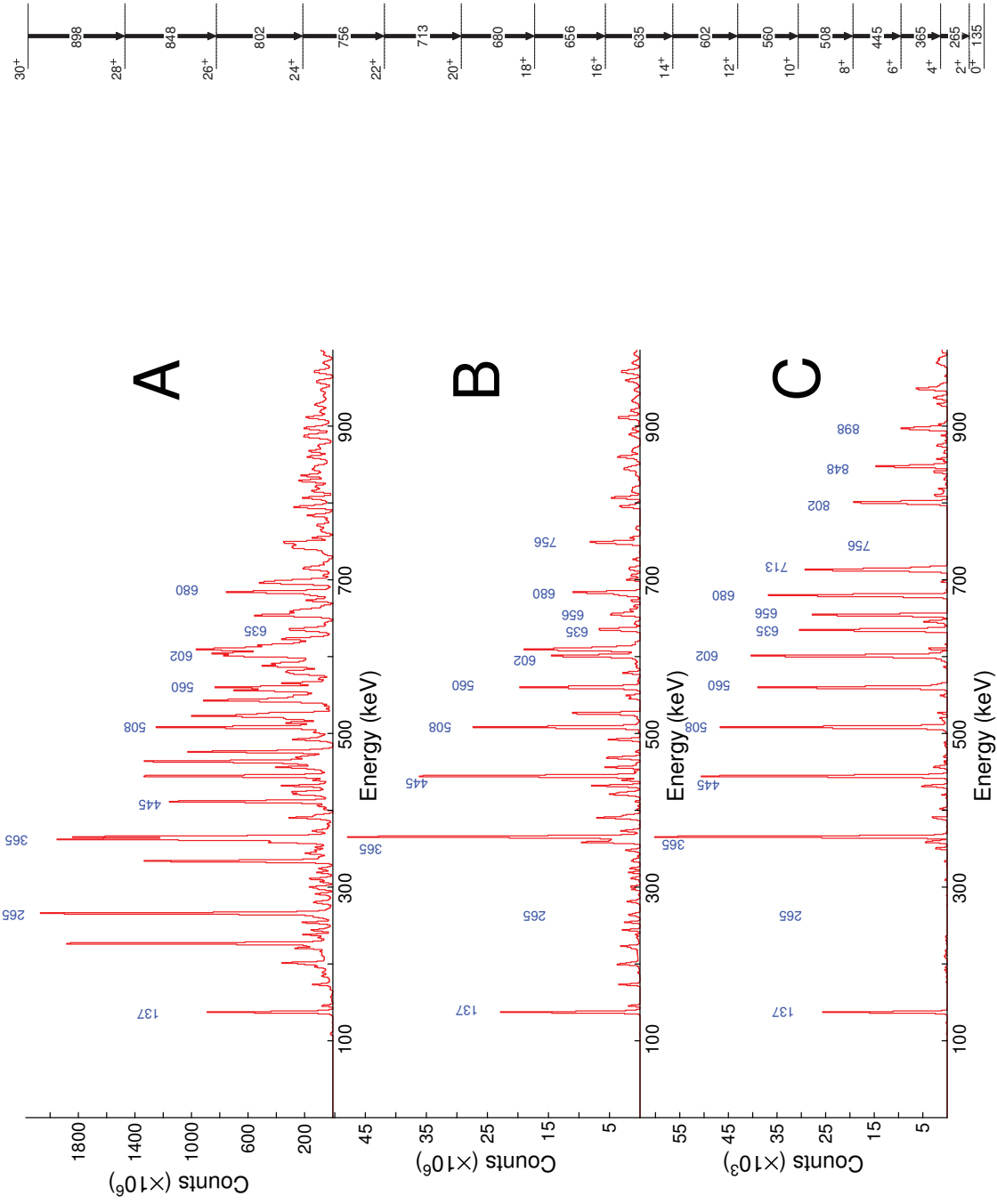


Figure 24: Example spectra of: (A) raw data, (B) the result of a gate on the 265-keV gamma, and (C) the result of a gate on the 265- and 756-keV gammas. The level scheme this information provides is shown on the right.



## 6.2 Level Scheme of $^{160}\text{Lu}$

The bulk of the initial work on this project involved piecing together the level scheme for all of the nuclei present in the data stream. Level schemes of various degrees of completion are already known for these nuclei, but due to the increased sensitivity Gammasphere offers, there is a chance to greatly expand on previous work. Figure 25 shows a sample spectrum of transitions within the  $\pi h_{11/2} \otimes \nu i_{13/2}$  band of  $^{160}\text{Lu}$  used to construct this level scheme. The starred gamma rays are previously-known transitions, while the peaks labeled to the right are evidence for the extension to the level scheme proposed in this work. Figure 26 shows the entire proposed level scheme for  $^{160}\text{Lu}$  constructed using spectra such as that shown in Figure 25. The boxed sections denote new additions to the level scheme not present in prior publications [3, 27, 28]. Bands 1-3 are three different configurations of the  $^{160}\text{Lu}$  nucleus which will be analyzed further Section 7.

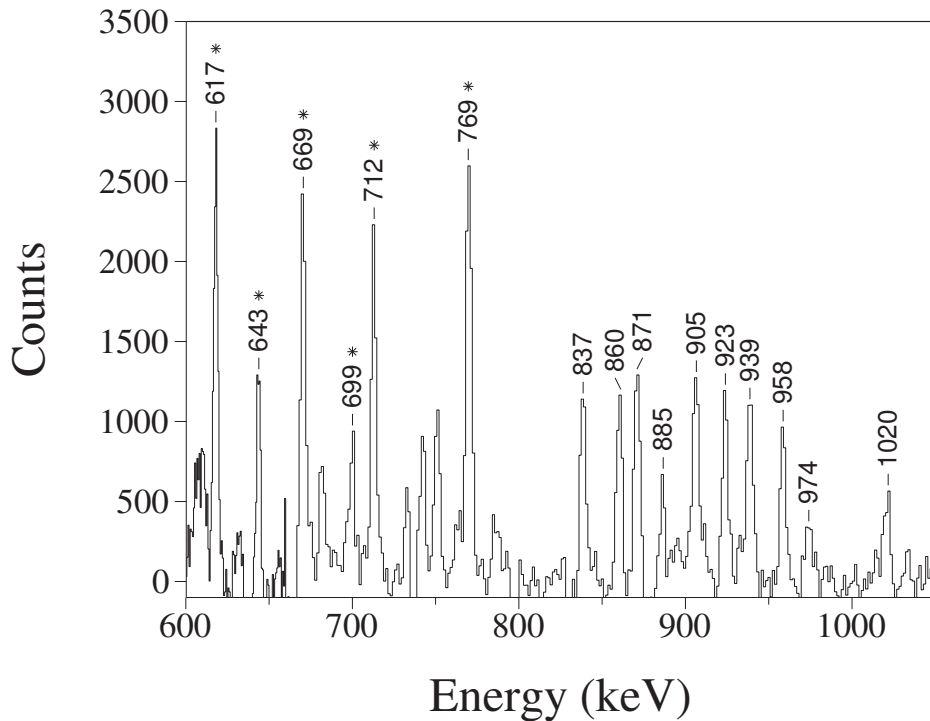


Figure 25: Example spectrum of the  $\pi h_{11/2} \otimes \nu i_{13/2}$  band of  $^{160}\text{Lu}$ . Spectra such as this one were used to construct the level scheme. The starred transitions were previously known. Note the higher energy peaks on the right side of the plot which are high-spin transitions within  $^{160}\text{Lu}$  that had not been seen before.

Note that, compared to the level scheme in Figure 23, the spins of the levels in Figure 26 are whole-integers rather than half-integers. This marks the difference between the odd-odd  $^{160}\text{Lu}$  nucleus and the odd-even  $^{161}\text{Lu}$  nucleus. Since  $^{160}\text{Lu}$  has an odd number of both neutrons and protons, there are at a minimum two unpaired particles. Since each particle has half-integer spin, the combination of two of these unpaired particles results in whole-integer spins.

Gamma rays, being a kind of electromagnetic radiation, can be classified by the polarization and orientation of the associated electric and magnetic fields. As discussed in Section 7, this classifi-

cation is useful in uniquely identifying configurations. The most commonly encountered classifications are electric quadrupoles (E2) and magnetic dipoles (M1) which are categorized by their interactions with matter and the pattern of emitted radiation. The nature of each type of transition manifests itself in the level scheme as changes in the *parity* of the band, which reflects the behavior of the wave function of the particle under spatial inversion, and changes in spin. An E2 transition changes spin by 2 but does not affect parity, and an M1 transition changes spin by 1 without changing parity. As such, in Figure 26 the E2 transitions are indicated by vertical lines (since parity does not change within a band) and M1 transitions are indicated by diagonal lines that connect bands of the same parity. Less frequently, there are linking transitions connecting bands of opposite parity. These transitions have an electric dipole (E1) nature.

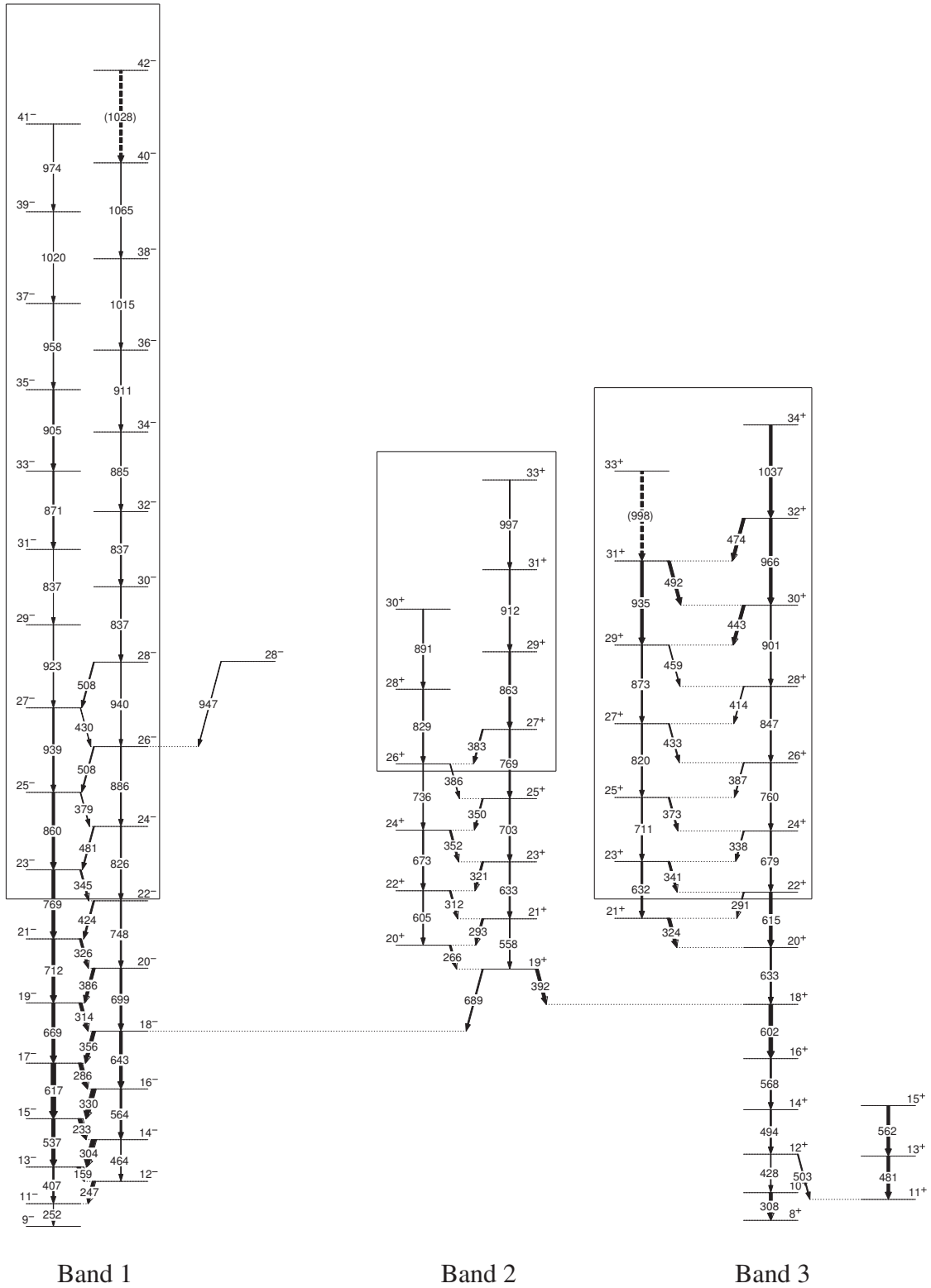


Figure 26: Proposed level scheme for  $^{160}\text{Lu}$  showing three different nuclear configurations. The boxed regions represent new progress in this work.

## 7 B(M1)/B(E2) Ratios

### 7.1 Theory

Excited states in nuclei have a variety of possible ways in which they can decay. The desired result is simply decreasing the excitation energy and spin, and any given state of a nucleus has a myriad of ways in which it can reach some state of lower energy. While any decay that is physically possible does indeed occur, the distribution of outcomes is governed by statistical likelihood—decays that are the most energetically favorable are the most likely to occur. Which decays are favorable is determined in large part by the configuration of the nucleus. That is to say, which particles are unpaired affects how the nucleus decays.

The mathematical representation of which decay mechanism is favored is called a *branching ratio*, or  $\lambda$ . The branching ratio is simply the ratio of the probability, expressed as a percentage, that a decay of a certain type happens to the total number of nuclei that decay. As an example, if the branching ratio for decay type A is 0.75, then out of 100 nuclei that have decayed, 75 of them decayed by type A.

When attempting to identify the configuration of the nucleus, particularly the new bands identified in the present work, it is particularly useful to define a related quantity called the reduced transition probability ratio, B(M1)/B(E2). Experimental values of the B(M1)/B(E2) ratio at each level of a decay sequence can then be compared to theoretical values calculated for a given nuclear configuration. The comparison of which configuration produces theoretical results most like the experimental results yields a reliable estimate of the actual configuration of the band.

### 7.2 Experimental Data

Experimental measurements of the B(M1)/B(E2) ratio were made by carefully selecting gates that returned the emissions of the level of interest without introducing extraneous data. This is accomplished by taking a gate with at least one gamma ray that is above the level for which the ratio will be calculated. Typically, these gates were the M1 transition out of the level above the level of interest and the M1 transition into the level of interest. This eliminates extraneous data from linked bands that feeds into the level in question. When this gate did not yield sufficient counts for the measurement, a gate consisting of a list of lower M1s with one of the M1s above the level usually produced an acceptably clean spectrum.

The B(M1)/B(E2) ratio was calculated for each efficiency-corrected spectrum by analyzing the area of the E2-transition peak and the M1-transition peak. After the energy and area of each peak were measured, the ratio follows from [18]:

$$\frac{B(M1)}{B(E2)} = \ln 2 \cdot \frac{E_\gamma(E2)^5}{E_\gamma(M1)^3} \cdot \frac{1}{\lambda} \quad (31)$$

where  $\lambda = \frac{I_\gamma(E2)}{I_\gamma(M1)}$  and uncertainties were propagated using partial derivatives.

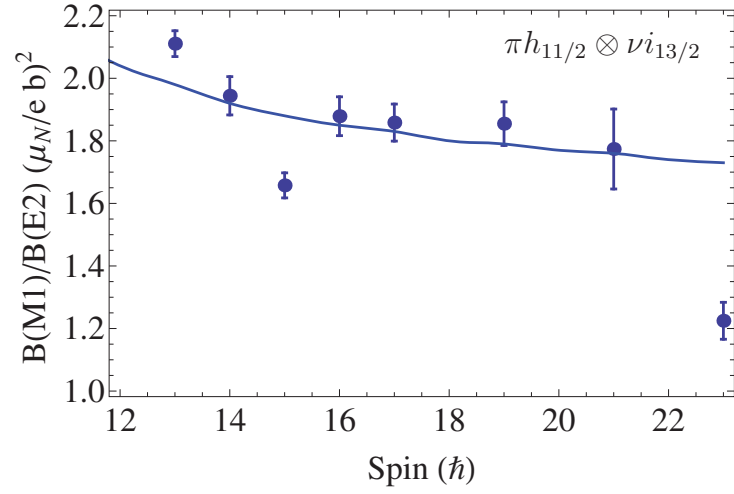
Such measurements were made using `gf3`, an analysis tool within RADWARE, for multiple levels in each strongly-coupled decay band of  $^{160}\text{Lu}$ . In theory, the  $B(M1)/B(E2)$  ratio should show a trend throughout the decay sequence. As seen in Figure 27, the values typically centered around definite values and are certainly distinct enough to tell each configuration apart. The plots in Figure 27 show the  $B(M1)/B(E2)$  ratio versus spin for a variety of states in each band. Error bars are applied to reveal the confidence of each data point. Outliers aside, Band 1 values tend to be just under  $2 \left(\frac{\mu_N}{e b}\right)^2$  and decrease with increasing spin, Band 2 hovered around  $3.5 \left(\frac{\mu_N}{e b}\right)^2$ , and Band 3 stayed near  $2.5 \left(\frac{\mu_N}{e b}\right)^2$  for most spins.

These values were calculated using experimental data. We must compare these results to theoretical calculations, shown as solid lines in Figure 27 to determine which unpaired particles exist within the various configurations.

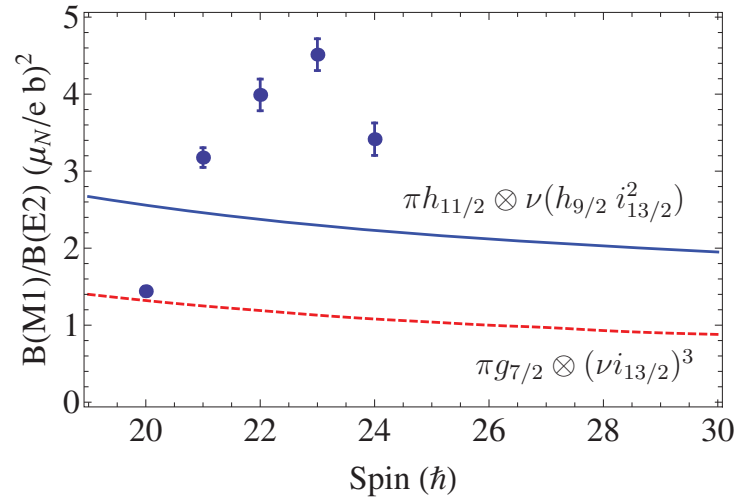
### 7.3 Theoretical Calculations

In order to identify the configuration of the nucleus that a given  $B(M1)/B(E2)$  ratio implies, we must make theoretical calculations of what the  $B(M1)/B(E2)$  ratio should be expected in a nucleus with a given configuration. As with much of nuclear physics, the ultimate determination of the configuration of the nucleus is whatever is energetically favorable for given conditions. Taking these conditions to be the deformation of the nucleus and the energy of the unpaired particle, we can utilize a plot of these parameters to roughly estimate the configuration of the nucleus. To do so requires the identification of which orbitals are closest to the Fermi surface. Such a plot is referred to as a *Nilsson diagram* [29]. There are separate Nilsson diagrams for protons and neutrons, as shown in Figure 28 and Figure 29, respectively.

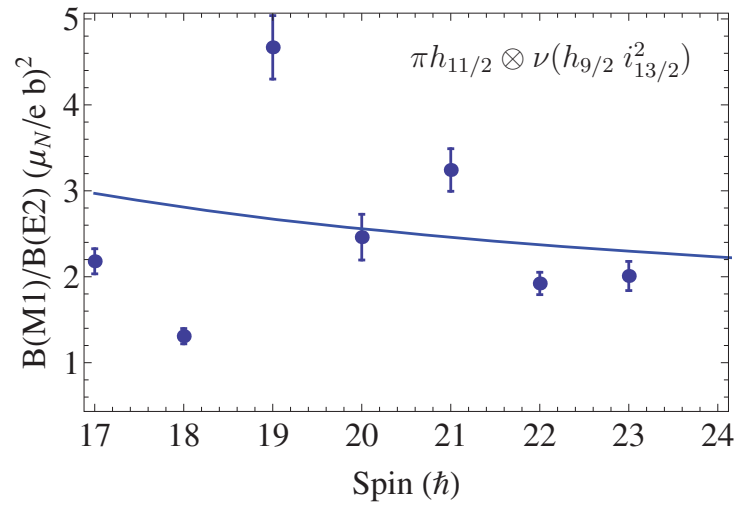
To estimate the Fermi surface, we first enter the graph on the  $x$ -axis by identifying a deformation parameter,  $\epsilon_2$ . For  $^{160}\text{Lu}$ , we can approximate  $\epsilon_2 = 0.2$ . Next, we count up to the number of nucleons the nucleus has, either 71 protons or 89 neutrons depending on whether we are using Figure 28 (for protons) or Figure 29 (for neutrons). The numbers on the figure represent gaps at the magic numbers, and each orbit of nucleons is doubly degenerate due to the pairing of particles, so each orbit that we cross adds two nucleons. By counting up to either 71 or 89 on the appropriate figure, we reach the Fermi level for either the protons or the neutrons in  $^{160}\text{Lu}$ . These levels are annotated by the intersecting lines on the Nilsson diagrams.



(a) Band 1



(b) Band 2



(c) Band 3

Figure 27: Branching ratio calculations for three bands of  $^{160}\text{Lu}$

Figure 28: Nilsson diagram for protons with  $50 \leq Z \leq 82$ . Lines have been overlaid to identify the Fermi surface of  $^{160}\text{Lu}$ . We are operating with a deformation of  $\epsilon_2 = 0.2$  and have  $Z = 71$ .

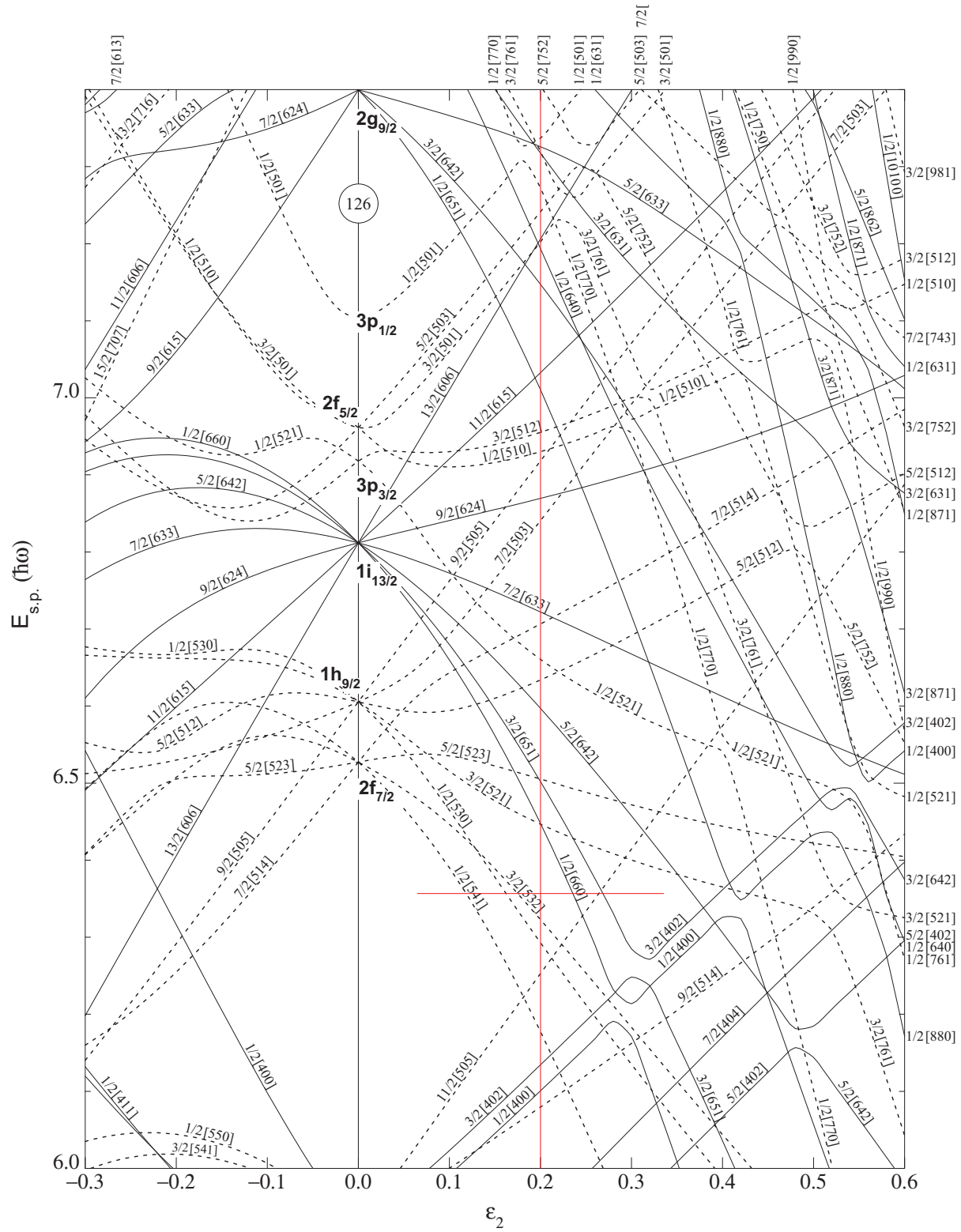


Figure 29: Nilsson diagram for neutrons with  $82 \leq N \leq 126$ . Lines have been overlaid to identify the Fermi surface of  $^{160}\text{Lu}$ . We are operating with a deformation of  $\epsilon_2 = 0.2$  and have  $N = 89$ .



As this is only a rough guess at the Fermi surface, and due to the fact that many of the orbitals are located very near one another, it is useful to test various configurations of the nucleons in the theoretical calculation to see which yields  $B(M1)/B(E2)$  ratios most like the experimental data. The process of these calculations is to determine the expected probability of M1 and E2 transitions then divide the two quantities. Before those calculations can be made, however, it is necessary to determine a number of nuclear properties.

Theoretical calculations utilized the shell model of a nucleus placed in a Woods-Saxon potential. Further, the wave function employed for theoretical calculations assumed a deformation of 0.2, resulting in a slightly prolate nucleus. Based on the characteristics of the unpaired particle coupled with this slight deformation, the model calculations allow us to identify a quantity called  $g_K$ , or the gyromagnetic ratio for the unpaired particle. The gyromagnetic ratio is the ratio of an object's magnetic moment (in essence, how strongly the object will react in a magnetic field) to that object's angular momentum.

For the purposes of deformed nuclei, there are two varieties of this ratio.  $g_K$ , as mentioned, is the gyromagnetic ratio of the unpaired particle in question, and  $g_R$  is the gyromagnetic ratio for the collective motion of the nucleus. That is to say, it describes the gyromagnetic ratio of everything else besides the unpaired particle.  $g_R$  will be constant for all work done in a given nucleus, since the total number of particles that exist in the nucleus outweighs the effects of unpairing different individual ones. A rule of thumb is that  $g_R$  is given by 70% of  $Z/A$ , which for  $^{160}\text{Lu}$  yields a value of 0.31.

Another quantity necessary for theoretical  $B(M1)/B(E2)$  calculations is the quadrupole moment of the nucleus. The quadrupole moment, or simply  $Q_0$ , is a description of how the charges within the nucleus are arranged and distributed. Since the deformation of the nucleus describes the distribution of the nucleons and consequently the distribution of the charge, the quadrupole moment can be found from just the radius and deformation of the nucleus:

$$Q_0 = \frac{3}{\sqrt{5}\pi} R^2 Z \beta (1 + 0.36\beta) \quad (32)$$

With the baseline information of  $Q_0$ ,  $g_K$ , and  $g_R$ , we can move onto a description of the specific configuration. For the theoretical calculations, the configurations are specified in terms of three values:  $g_K$ , as already discussed,  $\Omega$ , or the projection of the angular momentum of the nucleus along the symmetry axis, and a third quantity called alignment,  $i$ . Figure 9 illustrates several properties of a deformed nucleus with an unpaired nucleon orbiting about it.  $j$  is the total angular momentum of the particle orbiting at an angle  $\theta$  with respect to the symmetry axis  $z$ . The alignment,  $i$ , is the projection of the angular momentum along the rotational axis  $x$ . These values, summarized in Table 2, can be entered for all test configurations that were identified with the help of the Nils-son diagrams. After taking into account all of the specifications of the nuclear configuration, the reduced transition probability ratio is found by the following two formulae [18, 30, 21]:

$$B(E2 : I_i \rightarrow I_f) = \frac{5}{16\pi} e^2 Q_0^2 \langle I_i 2K0 | I_f K \rangle^2 \quad (33a)$$

Particle	$g_R$	$g_K$	$i$	$\Omega$
$\pi h_{11/2}$		1.34	3.8	3.5
$\pi g_{7/2}$		0.62	0	3.5
$\nu h_{9/2}$	0.31	-0.25	2.53	1.5
$\nu i_{13/2}$		-0.35	6.4	0.5
$(\nu i_{13/2})^2$		-0.35	10.8	0

Table 2: Summary of values used in theoretical B(M1)/B(E2) calculations for various unpaired particles which were pieced together into the various bands under consideration

$$\begin{aligned}
B(M1 : I \rightarrow I - 1) = & \frac{3}{8\pi I^2} \left\{ \sqrt{I^2 - K^2} [(1 - \Delta e' / \hbar \omega)(g_{K_1} - g_R)K_1 + \right. \\
& (g_{K_2} - g_R)K_2 + (g_{K_3} - g_R)K_3 + \dots] - \\
& \left. K[(g_{K_1} - g_R)i_1 + (g_{K_2} - g_R)i_2 + (g_{K_3} - g_R)i_3 + \dots] \right\}^2 \mu_N^2
\end{aligned} \tag{33b}$$

We performed branching ratio calculations for the three bands in  $^{160}\text{Lu}$ , as summarized by the solid lines in Figure 27. Our primary focus was the identification of the four unpaired particles in Band 2. Notice in Figure 26 that the lowest energy state in Band 2 is at a much higher spin than the lower energy state in Band 1. While Band 1 has only two unpaired particles, the extra “starting” energy of Band 2 supports the hypothesis that Band 2 has four unpaired particles. The extra 10  $\hbar$  units of spin are an additional indication that more than two particles are involved with Band 2.

Configurations are identified by a series of numbers which specify the type of unpaired particle, its orbital, and its angular momentum.  $\pi$  is used for protons and  $\nu$  is used for neutrons, with letters and fractions following to denote the particles orbital and angular momentum. Each band’s configuration is shown in Figure 27, but the two configurations of interest in Band 2 are  $\pi h_{11/2} \otimes \nu(h_{9/2} i_{13/2}^2)$  and  $\pi g_{7/2} \otimes (\nu i_{13/2})^3$ , henceforth referred to as configuration 1 and configuration 2, respectively. There is some level of dispute in published work as to the correct configuration of this band. We used configurations posited by two different papers for the nearby nucleus  $^{162}\text{Lu}$  as a starting point. Neighboring nuclei typically do not depart drastically from each other in their characteristics, so we can assume with a reasonable amount of certainty that the same band in neighboring nuclei will exhibit the same configuration.

Reference [32] argued for configuration 1 while Reference [31] put forth configuration 2. However, Reference [31] reached this conclusion by a different method than B(M1)/B(E2) ratios, and Reference [32] did not provide the parameters for their B(M1)/B(E2) calculations as we have done in Table 2. Accordingly, it was difficult to verify these works. Nonetheless, after testing theoretical calculations of both suggestions against experimental results, our data tend to support configuration 1. Both of these results are plotted on top of the experimental data in Figure 27. Although the data is by no means a perfect fit, our experimental values were clearly much higher than what configuration 2 predicts, with one outlier aside, the data is generally a decent match to configuration 1.

Interestingly, our theoretical calculations for Band 3 tend to support the idea that it has the same configuration as configuration 1 in Band 2. If this is the case, we would expect to see many

additional linking transitions between the two bands. On the other hand, it could be an indication that  $^{160}\text{Lu}$  is different enough from  $^{162}\text{Lu}$  that the configuration of Band 2 in  $^{162}\text{Lu}$  manifests itself as Band 3 in  $^{160}\text{Lu}$ .

## 8 Signature Splitting and Inversion

### 8.1 Signature Splitting

The Routhian's rotational invariance about the  $x$  axis allows for the existence of two closely related decay sequences known as rotational bands (see section 6.1 for more details on decay sequences). A given configuration of a nucleus (and consequently, a given wave function) can show two coupled decay sequences with energy levels that differ in  $I$  by  $1\hbar$ . Thus, if the spins of the bands are off by  $1\hbar$ , each band must have the opposite signature as demonstrated in section 3.4.1. Such interconnected bands are often referred to as signature pairs or signature partners.

However, each band of a signature pair will not necessarily have the same energy as its partner. The quantum number of signature arose when we considered the rotation of the spinning nucleus about the axis of rotation. In general, we would expect that the two signatures of an orbit would have similar energies. But, due to the Coriolis effect, this turns out not to be the case.

The Coriolis force in the nucleus is mathematically constrained to act between  $J$  and  $J + 1$  states. In all but one situation, the magnitudes of these paired states will be different ( $3/2$  and  $5/2$ ,  $7/2$  and  $9/2$ , etc.). The one exception is  $-1/2$  and  $1/2$ . That the magnitudes of these  $\Delta J = 1$  states are the same enables the admixing capability of the Coriolis force from a mathematical perspective. As the wave functions of neighboring states interact and mix, the nature of the  $\Omega = 1/2$  orbital can be successively transferred to higher orbits.

When this admixing is applied to the signature partners of a band, the alignment of one signature will increase while the alignment of the other will decrease. In other words, Coriolis admixing causes each signature partner to have a different energy: one energy will be shifted up, while the other will be shifted down. This phenomenon is known as *signature splitting*. Since Coriolis effects alter the nucleon's  $\Omega$ , it must also necessarily affect the energy of the orbit (since higher alignments requires more energy—see section 3.2). Thus, the fundamental splitting of the energies of the signature is caused by the  $\Omega = 1/2$  orbital, and the Coriolis force propagates that splitting into higher orbitals. We expect the down-shifted orbital to be energetically favored. For an odd-odd nucleus, this favored signature is given by:

$$\alpha_f = \frac{1}{2}(-1)^{j_\nu - 1/2} + \frac{1}{2}(-1)^{j_\pi - 1/2} \quad (34)$$

where  $j_\nu$  is the  $j$  of the neutron and  $j_\pi$  is the  $j$  of the proton. For the  $\pi h_{11/2} \otimes \nu i_{13/2}$  configuration that will be our primary focus, this equation gives  $\alpha_f = 0$ , meaning that even spins are favored.

### 8.2 Signature Inversion

In the 1980's, it was found that in a large number of  $A \approx 160$  the favored signature was actually higher in energy than its supposedly-unfavored partner. At some higher spin, known as the reversion spin, the signatures take on their expected orientation. Known as *signature inversion*,

this behavior has been studied extensively in the following years. The systematic study of Liu *et al.* [55] was critical to establishing this unusual phenomenon. In the following sections, we will discuss current theoretical explanations underlying signature inversion, present our systematic analysis of signature inversion in the  $A \approx 160$  region noting the predominant trends, and highlight the differences of two nuclei that surprisingly run counter to these trends— $^{160}\text{Lu}$  and  $^{162}\text{Ta}$ .

### 8.3 Signature Inversion Theory

There exists no universally accepted explanation of the underlying mechanism of signature inversion, though it is generally thought that such inversions of the expected favored signature band could be produced by a triaxial shape [35, 36, 37]. That being said, some physical alteration would have to occur in the nucleus as it transitions from high-spin to low-spin in order to produce the inversion as is seen. There are a handful of factors that can induce shape changes in a given nuclear configuration.

One such factor is the  $N$  and  $Z$  value of the nucleus with respect to the shell-gap sequence. We know that nuclei are very stable (that is to say, rigid in shape) when they have a magic number of nucleons, but nuclei are also “rigidly deformed” when their nucleons are half-way between magic numbers. Such mid-shell nuclei exhibit strong prolate and oblate deformations. However, nuclear deformations becomes less rigid if they are relatively close (6-8 nucleons) from a magic number. Such nuclei are precisely the transitional nuclei studied in this work.

Since transitional nuclei are neither spherical nor strongly deformed from the total number of nucleons, their shape is much more susceptible to the shape-driving effects of the unpaired particles as opposed to the collective nuclear structure. Such nuclei are referred to as being *soft* as they are more greatly influenced by these effects than rigid nuclei.

The  $\nu i_{13/2}$  neutron has been closely associated with the phenomenon of signature inversion and is observed in the configurations of nearly all  $A \approx 160$  nuclei that show an inversion. This neutron has been thought to generally drive towards positive triaxial deformation in nuclei. This is the  $\gamma$  parameter that was briefly mentioned in section 3.2. Recall that whereas quadrupole deformations leave a symmetry axis (think of the long axis of a football), triaxial deformations deform the nucleus along all three axes.

Thus, the general thought is that the  $\nu i_{13/2}$  neutron could be producing triaxial deformations in soft nuclei at low spins. Indeed, *CSM calculations predict that the signature ordering should invert at low spin in nuclei with positive  $\gamma$  deformation* [35]. At higher spins, however, the Coriolis force stiffens the quadrupole (versus triaxial) shape of the nucleus that allows the expected signature-dependent energy arrangement of the bands.

### 8.4 Experimental Data

Figure 30 consolidates the systematics employed in our analysis and will be referred to heavily in the following section. In this figure, the signature splitting of the  $\pi h_{11/2} \otimes \nu i_{13/2}$  bands for odd-odd nuclei in the  $A \approx 160$  region are plotted. The signature splitting parameter can be defined as:

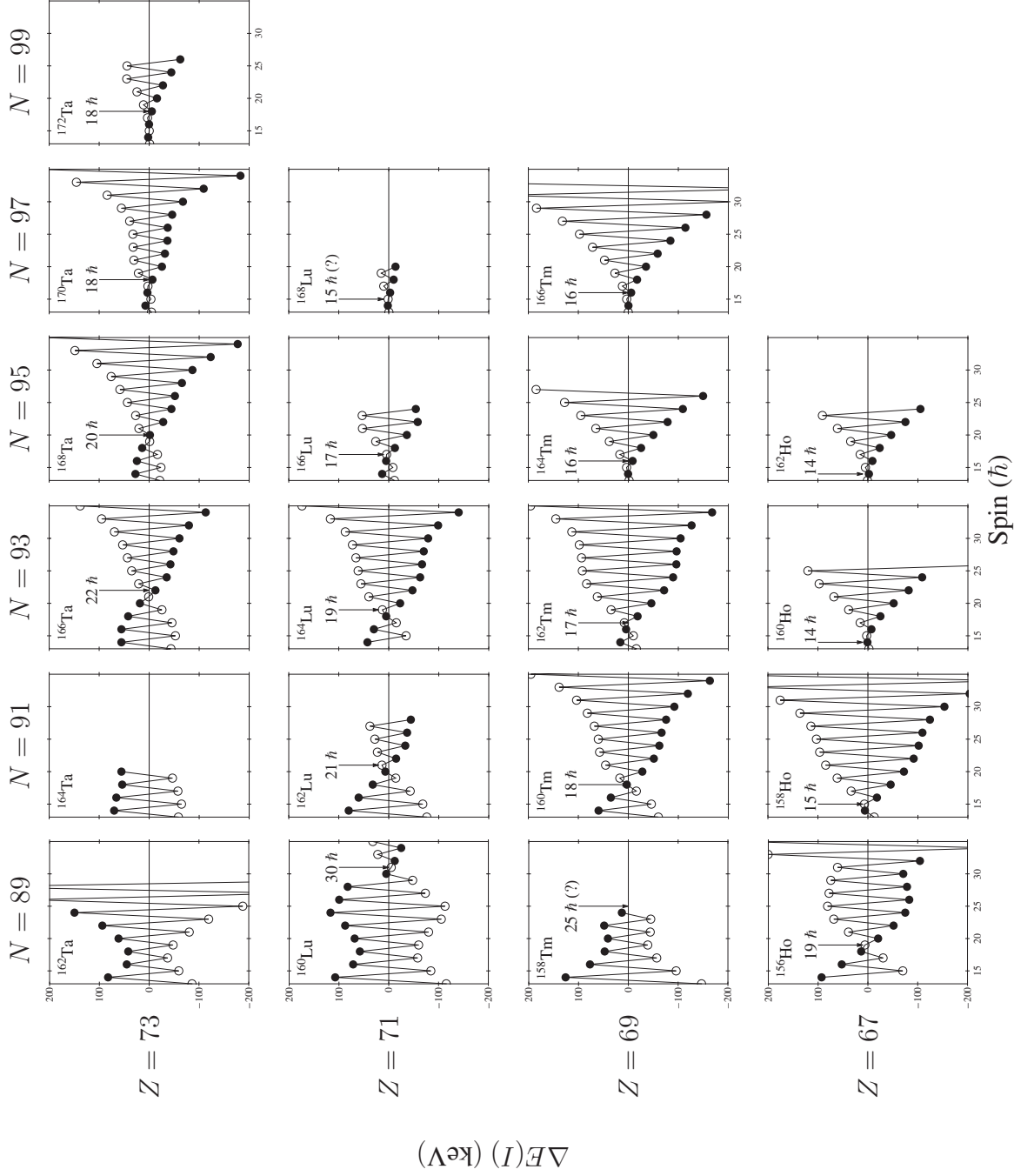


Figure 30: Signature splitting systematics for  $A \approx 160$  nuclei. Filled circles correspond to  $\alpha = 0$  while open circles correspond to  $\alpha = 1$ . Data taken from references [38]-[54].

$$\Delta E(I) = E(I) - E(I - 1) - \frac{(E(I + 1) - E(I) + E(I - 1) - E(I - 2))}{2} \quad (35)$$

The solid circles represent the even-spin ( $\alpha = 0$ ) sequences, which are expected to be lower in energy, while the open circles represent the odd-spin ( $\alpha = 1$ ) sequence. Note that, even though we demonstrated that even spins are expected to be favored, the even spins initially have higher energy than the odd spins. This ordering reverts at the reversion spin which has been annotated in each case that it was seen.

The systematic observation of signature splitting in  $A \approx 160$  nuclei has yielded a few empirical observations that we will explore in detail [55]. As we analyze these effects, keep in mind the interplay between the shape driving effects of soft, transitional nuclei and the Coriolis force.

#### 8.4.1 Trends within chains of isotopes

Within a chain of isotopes, that is, for a given  $Z$ , we see that the reversion spin decreases as  $N$  increases. For instance, working from left to right within  $Z = 69$  (isotopes of thulium), the reversion spins follow the sequence  $25 \hbar$ ,  $18 \hbar$ ,  $17 \hbar$ ,  $16 \hbar$ ,  $16 \hbar$  as  $N$  increases from 89 to 97. This follows from our triaxial explanation of signature inversion. The two magic numbers closest to this region are 82 and 126. As  $N$  increases from 89, it moves closer to the mid-shell gap at 104. As the isotopes near  $N = 104$ , they become more rigid and resistant to the effects of the single unpaired nucleons. As a result, the  $\gamma$  deformation is lessened and it takes a lower amount of Coriolis force (generated by a lower amount of rotation) to overcome the triaxial deformation.

This argument is strengthened by the observation that the absolute magnitude of the signature splitting also decreases as  $N$  increases. Note that for  $^{158}\text{Tm}$  the splittings are  $\approx \pm 100 \hbar$  though for  $^{164}\text{Tm}$  they are nearly of imperceptible magnitude before the reversion occurs. We would expect the signature splitting to be less extreme for a less  $\gamma$  deformed nuclei, which those with higher  $N$  presumably are by this line of reasoning.

#### 8.4.2 Trends within chains of isotones

Within a chain of isotones, that is, for a given  $N$ , we see that the reversion spin increases as  $Z$  increases. Working from bottom to top within  $N = 93$ , we observe that the reversion spins follow the sequence  $14 \hbar$ ,  $17 \hbar$ ,  $19 \hbar$ ,  $22 \hbar$  as  $Z$  increases from 67 to 73. Once again, this trend meshes nicely with the triaxial understanding of signature inversion. For the protons, the two nearest magic numbers are 50 and 82 with the mid-shell gap at 66. Thus, we have the opposite situation as with the trends within isotopes. At  $Z = 67$ , we start essentially at the mid-shell gap where the nuclei are rigidly deformed. As  $Z$  moves into the transitional region, the nucleus becomes softer and more influenced by the  $\gamma$  deformation produced by the  $\nu i_{13/2}$  neutron. Consequently, a greater amount of Coriolis force which requires a greater rotational velocity is needed to mask the triaxiality and restore the expected ordering.



The magnitude of signature splitting again supports our hypothesis. If the isotones are truly becoming softer and more triaxial as  $Z$  increases, then we should expect the magnitude of the signature splitting to increase along with  $Z$ . We note that the splitting magnitudes in  $^{160}\text{Ho}$  are close to zero before the reversion, though those in  $^{166}\text{Ta}$  are of the order  $\approx \pm 50 \hbar$ .

### 8.4.3 Decrease of signature splitting magnitude

Our additional trend worth discussing is that the magnitude of signature splitting should decrease leading up to the reversion spin, before increasing afterward. Examine the signature splitting plot of  $^{166}\text{Ta}$  as an example. At the lowest spins, the signature splitting is roughly 50 keV. Just prior to the reversion at  $22 \hbar$ , the magnitude decreases to  $\approx 15$  keV. After the reversion spin, the magnitude remains at  $\approx 15$  keV before increasing approximately quadratically up to 150 keV at the highest observed spin.

The cause of this “necking down” of the splitting magnitude around the reversion spin is ultimately a result of the balance of competing effects within the nucleus. Namely, these effects are  $\gamma$  deformation that leads to signature inversion and the Coriolis force which favors the normal energy ordering. At the lowest spins, the triaxial-driving effects of the  $i_{13/2}$  neutron are the most influential since the magnitude of the Coriolis force is smallest. As such, we would expect the signature inversion to be the greatest when the nucleus is not affected by Coriolis effects at low spins.

At the reversion frequency, the Coriolis force overpowers the  $\gamma$  deformation sufficiently to restore the normal energy ordering, but that is not to say that triaxiality is completely banished from the nucleus. Rather, it will always be present so long as the  $i_{13/2}$  neutron remains an unpaired particle. However, its influence will become increasingly small as higher spins produce even greater Coriolis effects. This explains the gradual increase in the energy gap between the signature partners after the reversion spin.

We can summarize the conclusions of our systematics with three rules:

1. For a given  $Z$ , as  $N$  increases, the reversion spin decreases.
2. For a given  $N$ , as  $Z$  increases, the reversion spin increases.
3. For a given  $Z$ , the magnitude of the signature splitting at low spin decreases as  $N$  increases.

## 8.5 Exceptions to the trends

Despite the general agreement of the nuclei in Figure 30 to the systematics just presented, two nuclei dramatically depart from these trends. These nuclei are  $^{162}\text{Ta}$  [38] and  $^{160}\text{Lu}$  located in the upper-left two plots of Figure 30. Due to our present work,  $^{160}\text{Lu}$  has been observed at high enough spins to allow for a complete analysis of its signature inversion qualities.  $^{162}\text{Ta}$  has enough of a foundation that we can compare it to  $^{160}\text{Lu}$  but not enough to fully analyze in its own right. As such, we will focus on the anomalies seen in  $^{160}\text{Lu}$ .



There are two interesting phenomena seen in  $^{160}\text{Lu}$ . The first is its exceptionally high reversion spin of  $30 \hbar$ —significantly greater than the next highest reversion spin in the systematics. The second is the initial necking down around  $17 \hbar$  that is not accompanied by the reversion spin. The first quarter of the signature splitting plot looks entirely consistent with the rest of the schematic. The magnitude begins decreasing as spin increases, and it appears as though the magnitude bottleneck is heading towards a reversion spin at  $\approx 23 \hbar$ . In fact, if this were to be the case,  $^{160}\text{Lu}$  would perfectly fall in line with the other trends. Its hypothetical reversion spin of  $23 \hbar$  would be the highest within the lutetium isotopes, as expected for it being the most neutron-rigid nucleus, and it would be on course within the  $N = 89$  isotones for being a proton-soft nucleus.

However, some additional physical phenomenon intervenes to delay the reversion spin a considerable amount. Similar behavior is evident in  $^{162}\text{Ta}$ , though the actual reversion spin has not yet been observed. Nonetheless, we do see the bottle neck approach a reversion spin of around  $25 - 30 \hbar$  before the signature inversion becomes reinforced. As  $^{160}\text{Lu}$  and  $^{162}\text{Ta}$  are neighboring nuclei, it is reasonable to suspect that the same physics affects the signature splitting of each.

## 9 Description of $^{160}\text{Lu}$

### 9.1 Alignment Gain and EF Transition

To attempt an explanation for the unusual signature inversion in  $^{160}\text{Lu}$ , we explored the alignment gains in the  $\pi h_{11/2} \otimes \nu i_{13/2}$  bands of  $N = 89$  nuclei in this region. The resulting plots are shown in Figure 31. Recall that alignment is the component of the total angular momentum of the unpaired particles along the axis of rotation.

All four of these nuclei show at least the beginnings of an alignment gain towards the end of the plotted bands, if not a substantial gain. This corresponds to the  $BC$  crossing. However,  $^{160}\text{Lu}$  and  $^{162}\text{Ta}$  also show an additional gain of  $\approx 4 \hbar$  around  $\hbar\omega = 0.25 \text{ MeV}$ . This cusp, denoted by the vertical line in Figure 31, is absent in the lower- $Z$  nuclei. We believe that this alignment gain is the  $EF$  crossing which subsequently has a substantial impact on the signature splitting dynamics of these nuclei.

The evidence for our observation of the  $EF$  crossing comes from a study conducted by Hübel *et al.* [23] of various excitation bands in the neighboring even-even nucleus  $^{162}\text{Hf}$ . Recall that we studied  $^{162}\text{Hf}$  earlier in section 3.4.3 when we first presented the idea of band crossings. As an even-even nucleus, the ground state configuration of  $^{162}\text{Hf}$  has quasiparticles (QPs) in all of the negative-energy trajectories and holes in the positive energy trajectories. Thus, as a particle in the  $-E$  trajectory approaches the interaction region with the positive-energy  $F$  orbital, it can cross into the positive-energy trajectory resulting in an alignment gain.

If, however, we consider a rotational band of  $^{162}\text{Hf}$  that already has either the  $E$  or  $F$  orbital occupied (specifically, the  $AE$  and  $AF$  configurations), we observe a different result. Take the  $AE$  case. As the particle in the  $-F$  orbital approaches the  $EF$  crossing, it meets the particle in the  $E$  orbital rather than the hole it saw in the ground state case. As such, the  $EF$  crossing is blocked in these bands and we see no such alignment gain.

This phenomenon is shown in Figure 32. The first major backbend in the ground state band is the  $AB$  crossing. For the  $AE$  and  $AF$  bands, the initial upper-left movement shows the breaking of ground state pairs and the establishment of these bands as two-particle systems. Thus, we have three comparable two-particle bands:  $AB$ ,  $AE$ , and  $AF$ . Note that as spin increases, the  $AE$  and  $AF$  bands show virtually no alignment gain from  $\approx 0.2 - 0.4 \text{ MeV}$ . The  $AB$  band, however, gradually increases in alignment through this region. The only explanation for the difference in behavior is that the  $EF$  crossing is allowed for the  $AB$  band but is blocked in  $AE$  and  $AF$ .

Admittedly,  $^{162}\text{Hf}$  is somewhat of a different nucleus than  $^{160}\text{Lu}$  and  $^{162}\text{Ta}$  since it is even-even. However, after the  $^{162}\text{Hf}$  nucleus goes through both the  $AB$  crossing and the  $EF$  crossing, it adopts the four-QP configuration  $ABEF$ . Should  $^{160}\text{Lu}$  undergo the  $EF$  transition as we propose it does, it also would show a four-QP configuration based on the  $EF$  nucleons as well as its ground state unpaired nucleons ( $\pi h_{11/2} \nu i_{13/2}$ ). Though the analogy is not without room for error, we believe that there is no explanation for the alignment gain seen in  $^{160}\text{Lu}$  and  $^{162}\text{Ta}$  other than the  $EF$  crossing. The observation of that crossing in the nearby nucleus  $^{162}\text{Hf}$  provides a substantial piece of supporting evidence that the  $EF$  crossing plays a role in this region.

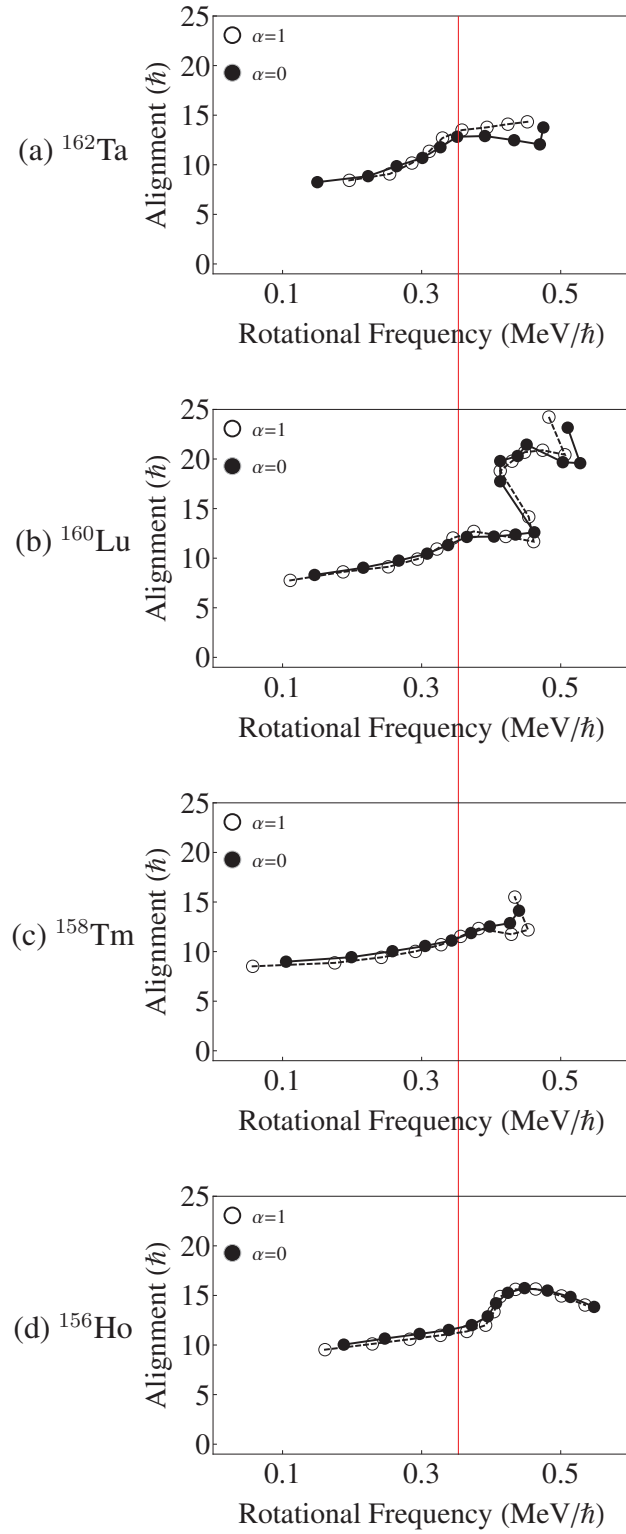


Figure 31: Alignment plots for the  $\pi h_{11/2} \nu i_{13/2}$  bands in the odd-odd,  $N = 89$  Ho, Ta, Lu, and Ta nuclei. Plots were created using Harris Parameters of  $I_0 = 12$  and  $I_2 = 90$ .

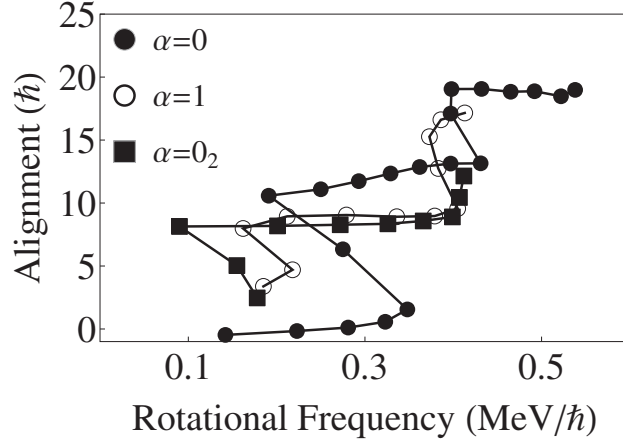


Figure 32: Alignment plots for bands in  $^{162}\text{Hf}$ . The hollow circle and square markers show the  $AE$  and  $AF$  bands respectively, while the solid circle shows the  $AB$  band. Note that, between 0.2 and 0.4 MeV of rotational energy, the  $AB$  band increases in alignment while the  $AE$  and  $AF$  bands do not. This is a product of the blocked  $EF$  crossing in the latter two bands.

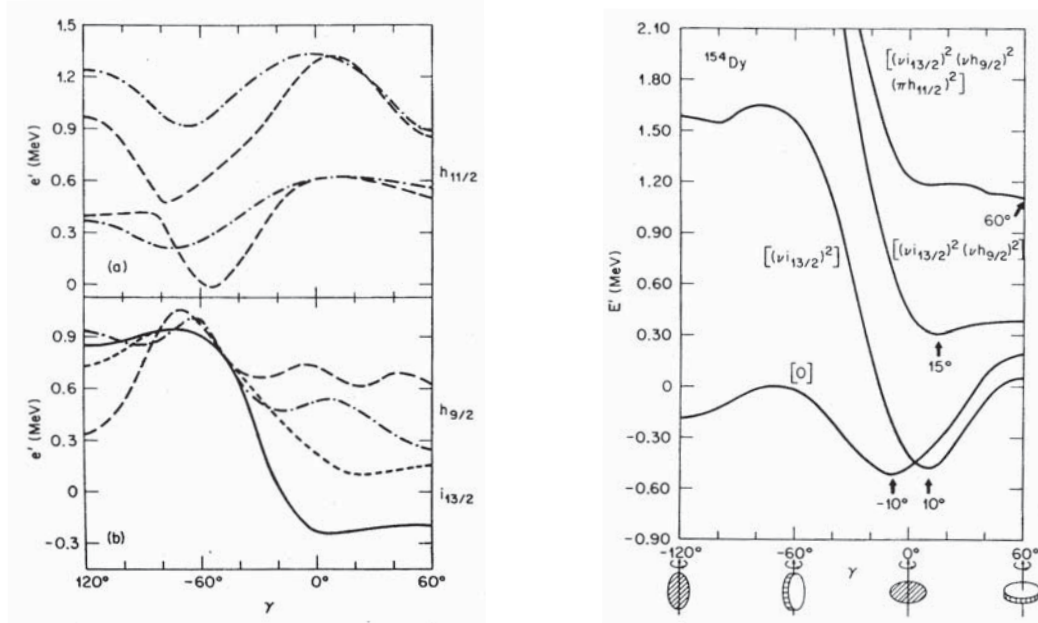
## 9.2 Shape-Driving Effects of the EF Crossing

Having established the presence of the  $EF$  crossing in the  $\pi h_{11/2} \otimes \nu i_{13/2}$  band of  $^{160}\text{Lu}$ , we must explore the implications of the unpairing of those nucleons on the shape of the nucleus, and ultimately the atypical signature inversion they exhibit. As discussed in section 8.3, one well-supported hypothesis of the origin of signature inversion is triaxial shape deformation ( $\gamma$ ). At lower spins, the shape-driving effects of individual nucleons is the dominant factor. Only at higher spins can Coriolis effects overwhelm the influence of individual nucleons. Thus, for most nuclei, once the Coriolis forces take over, the expected ordering of the signature partners is restored. However, as we have discussed, this restoration is delayed in the two nuclei we are focusing on.

Figure 33 shows theoretical predictions for the  $\gamma$  driving tendencies of certain nucleons. Figure 33a focuses on individual nucleon orbitals, while Figure 33b highlights these effects for entire configurations. In these plots, the  $y$ -axis represents the overall energy of the configuration versus the amount of  $\gamma$  deformation along the  $x$ -axis. In general, nature tends to prefer whichever lowest energy option is available. Thus, we expect the lowest point on these curves to be observed in reality.

The four-QP configuration, similar to a post- $EF$  crossing  $^{160}\text{Lu}$  configuration, is labeled as  $(\nu i_{13/2})^2 (\nu h_{9/2})^2$  in Figure 33b. Since this curve has its absolute minimum located at  $\gamma = 15^\circ$ , we know that the energy of this four-QP configuration is the lowest at  $15^\circ$  of  $\gamma$  deformation. Accordingly, we expect that this configuration will preferentially drive the nuclear shape towards this deformation parameter.

Next, we can confirm this behavior by examining the constituent nucleons of that four-QP band in Figure 33a. Specifically, we are looking at the  $i_{13/2}$  and the  $h_{9/2}$  neutrons. Although the effect is somewhat less obvious than the trend for the configuration as a whole, we can see that the lines



(a) Illustration of the shape-driving effect of individual nucleons in specific orbitals.

(b) Illustration of the effect of  $\gamma$  deformation on the energies of configurations in  $^{154}\text{Dy}$ . The absolute minimum of each curve corresponds to the value of  $\gamma$  expected. The  $(\nu i_{13/2})^2$  configuration drives the nuclear shape towards  $\gamma = 10^\circ$ , while the  $(\nu i_{13/2})^2(\nu h_{9/2})^2$  configuration drives toward  $\gamma = 15^\circ$ .

Figure 33: Shape-driving effects of nucleons [56].

for these two nucleons are trending towards lower energy at higher  $\gamma$  deformation. Again, this supports our argument that the unpairing of  $EF$  contributes additional triaxiality to the shape of the nucleus.

Since we know that the transitional nuclei are softer than mid-shell nuclei, specifically in that they are more susceptible to the shape-driving effects of given nucleons, these nuclei are likely to be more affected by the triaxial tendencies of the  $EF$  crossing. It appears that, in the two transitional nuclei, the  $EF$  crossing occurs even before the expected signature inversion frequency, thus imparting additional triaxiality and prolonging the effects of the inversion. For the rest of the nuclei in our systematics, the crossing happened after Coriolis effects had already dominated the shape of the nuclei and thus similar patterns were not observed. This explains the initial necking down of the signature inversion—the nucleus begins by behaving normally, then the  $EF$  crossing alters the shape of the nucleus in a way that increases the magnitude of the signature inversion. We now have four QP's all driving the nucleus towards positive triaxiality which requires an even stronger amount of Coriolis force (generated at a higher spin) to overcome. The other  $A \approx 160$  nuclei simply undergo the reversion before the  $EF$  crossing, which causes the relatively minor  $EF$  crossing to be entirely masked by the combination of the rigidly deformed nucleus and strong Coriolis forces.

## 10 Conclusion

Our look at the odd-odd nucleus  $^{160}\text{Lu}$  was motivated principally by a desire to more closely observe a nucleus in the transitional region between magic nuclei and mid-shell gap nuclei. We employed the high-resolution capabilities of ANL's Gammasphere to significantly expound upon the knowledge of the ground state band of  $^{160}\text{Lu}$ , in addition to more fully describing two additional bands. Using  $B(M1)/B(E2)$  ratio calculations, we assigned the bands the respective configurations of  $\pi h_{11/2} \otimes \nu i_{13/2}$ ,  $\pi h_{11/2} \otimes \nu(h_{9/2} i_{13/2}^2)$ , and  $\pi h_{11/2} \otimes \nu(h_{9/2} i_{13/2}^2)$ .

We continued our analysis by looking at the systematics of signature inversion in the  $A \approx 160$  region, and determined that  $^{160}\text{Lu}$  exhibited unusual behavior when compared with its neighbors. We used experimental alignment information along with theoretical CSM calculations to investigate the cause of the delayed inversion and propose that it is due to extra triaxiality imparted on the nucleus by the unpairing of  $h_{9/2}$  neutrons. Since  $^{160}\text{Lu}$  is a transitional nucleus and its shape is more greatly influenced by individual nucleons, this effect is masked in its more rigid neighbors.

## References

- [1] S. W. Ødegård *et al.*, Phys. Rev. Lett. **86**, 5866 (2001).
- [2] E. S. Paul *et al.*, Phys. Rev. Lett. **98**, 012501 (2007).
- [3] L. L. Wang *et al.*, Chin. Phys. Lett. **29**, 062103 (2012).
- [4] L.M. Bollinger Ann. Rev. Nucl. Part. Sci. **36**, 475 (1986).
- [5] R.V.F. Janssens and F.S. Stephens Nucl. Phys. News **6**, 9 (1996).
- [6] K.W. Shepard *et al.*, IEEE Trans. Nucl. Sci. **NS-24**, 1147 (1977).
- [7] K. S. Krane, *Introductory Nuclear Physics*. (John Wiley & Sons, Hoboken, 1988).
- [8] V. Blacus, Wikimedia Commons.  
<http://commons.wikimedia.org/wiki/File:Electromagnetic-Spectrum.svg>
- [9] *The Nobel Prize in Physics 1921*.  
[http://www.nobelprize.org/nobel\\_prizes/physics/laureates/1921/index.html](http://www.nobelprize.org/nobel_prizes/physics/laureates/1921/index.html)
- [10] R. Nave, *Compton Scattering*. Georgia State University Hyperphysics.  
<http://hyperphysics.phy-astr.gsu.edu/hbase/quantum/comptint.html>
- [11] A. Aguilar, *High-Spin Nuclear Structures of  $^{168,170}\text{Ta}$  and Triaxial Strongly Deformed Structure in  $^{160}\text{Yb}$* . Ph.D. thesis, Florida State University, 2008.
- [12] M.J. Berger *et al.*, *XCOM: Photo Cross Section Database* (version 1.5)  
<http://physics.nist.gov/xcom>
- [13] D. J. Wagner, *Glossary for Semiconductors*. Rensselaer Polytechnic Institute.  
[http://www.rpi.edu/dept/phys/ScIT/InformationProcessing/semicond/sc\\_glossary/scglossary.htm](http://www.rpi.edu/dept/phys/ScIT/InformationProcessing/semicond/sc_glossary/scglossary.htm)
- [14] J. K. Shaw and R. E. Faw, *Fundamentals of Nuclear Science and Engineering* (CRC Press, 2008).
- [15] R.D. Woods and D.S. Saxon, Phys. Rev. **95** 2, 577 (1954).
- [16] R.F. Casten, *Nuclear Structure from a Simple Perspective* (Oxford University Press, 1990).
- [17] S.G. Nilsson, Dan. Mat. Fys. Medd. **29**, no. 16 (1955).
- [18] A. Bohr and B.R. Mottelson, *Nuclear Structure*, volume II. (World Scientific Pub. Co., 1998).
- [19] V.G. Soloviev, trans. P. Vogel, *Theory of Complex Nuclei* (Pergamon Press, 1976).
- [20] R.B. Firestone *et al.*, *Table of Isotopes, 8th Edition*. (John Wiley & Sons, New York, 1996).
- [21] S. Frauendorf, Phys. Lett. **100B**, 219 (1981).

- [22] S. C. Pancholi, *Exotic Nuclear Excitations*, (Springer Science, 2011).
- [23] H. Hübel *et al.*, Z. Phys. A **329**, 289 (1988).
- [24] D. Radford, Nucl. Instrum. Methods Phys. Res. **A361**, 297 (1995).
- [25] M. Cromaz *et al.*, Nucl. Instrum. Methods Phys. Res. **A462**, 519 (2001).
- [26] P. Bringel *et al.*, Eur. Phys. J. A **24**, 167 (2004).
- [27] L. Yin *et al.*, Eur. Phys. J. A **11**, 379 (2001).
- [28] H. Sun *et al.*, Z. Phys. **A341**, 241 (1995).
- [29] S. G. Nilsson *et al.*, Nucl. Phys. **A131**, 1 (1969).
- [30] F. Dönau, Nucl. Phys. **A471**, 469 (1987).
- [31] M. A. Cardona *et al.*, Phys. Rev. C **56**, 707 (1997).
- [32] S. L. Gupta *et al.*, Phys. Rev. C **56**, 1281 (1997).
- [33] R. Bengtsson and S. Frauendorf Nucl. Phys. **A327**, 139 (1979).
- [34] Y. Liu *et al.*, Phys. Rev. C **54**, 719 (1996).
- [35] R. Bengtsson *et al.*, Nucl. Phys. **A415**, 189 (1984).
- [36] A. Ikeda and T. Shimano Phys. Rev. Lett. **63**, 139 (1989).
- [37] A. Ikeda and T. Shimano Phys. Rev. C **42**, 149 (1990).
- [38] F.G. Moradi *et al.*, Phys. Rev. C **84**, 064312 (2011).
- [39] D.G. Roux *et al.*, Phys. Rev. C **65**, 014308 (2002).
- [40] D.J. Hartley *et al.*, Phys. Rev. C **82**, 057302 (2010).
- [41] A. Aguilar *et al.*, Phys. Rev. C **81**, 064317 (2010).
- [42] D. Hojman *et al.*, Phys. Rev. C **61**, 064322 (2000).
- [43] P. Bringel *et al.*, Phys. Rev. C **75**, 044306 (2007).
- [44] G. Zhao *et al.*, Eur. Phys. J. A **9**, 299 (2000).
- [45] S.K. Katoch *et al.*, Eur. Phys. J. A **4**, 307 (1999).
- [46] M. A. Riley *et al.*, Phys. Rev. C **39**, 291 (1989).
- [47] K. Lagergren *et al.*, Phys. Rev. C **72**, 057303 (2005).
- [48] J.M. Espino *et al.*, Nucl. Phys. **A640**, 163 (1998).
- [49] W.Reviol *et al.*, Phys. Rev. C **59**, 1351 (1999).
- [50] M.A. Cardona *et al.*, Phys. Rev. C **66**, 044308 (2002).
- [51] D.M. Cullen *et al.*, Phys. Rev. C **57**, 2170 (1998).



- [52] C. H. Yu *et al.*, Bulletin of the American Physical Society **40(2)**, 1005e (1995).
- [53] S. Drissi *et al.*, Nucl. Phys. **A600**, 63 (1996).
- [54] E. Escrig *et al.*, Eur. Phys. J. A **21**, 67 (2004).
- [55] Y. Liu *et al.*, Phys. Rev. C **52**, 2514 (1995).
- [56] Y. S. Chen *et al.* Phys. Lett. B **171**, 7 (1986).